/
Article / Book Information

Title	Experimental study on suffusion under multiple seepages and its impact on undrained mechanical responses of gap-graded soil
Authors	Jitrakon Prasomsri, Akihiro Takahashi
Citation	Soils and Foundations, Vol. 61, Issue 6, pp. 1660-1680
Pub. date	2021, 12

Technical Paper

Experimental study on suffusion under multiple seepages and its impact on undrained mechanical responses of gap-graded soil

Jitrakon Prasomsri, Akihiro Takahashi[*]

Department of Civil and Environmental Engineering, Tokyo Institute of Technology, Tokyo, Japan

Abstract

An experimental investigation of multiple seepage-induced suffusion and its impact on the mechanical responses of internally unstable gap-graded soil, with a fines content of 25%, is presented in this paper. Using a modified triaxial erosion apparatus, with a redesigned seepage control system, erosion tests under multiple seepage conditions, as well as undrained monotonic and cyclic compression tests, are performed. It is found that multiple seepages cause an eroded mass without a marked change in volume and with a change in hydraulic conductivity as the number of seepage cycles increases. The monotonic compression tests show that eroded soil presents a smaller peak strength, residual strength, and a greater contractive response than non-eroded soil. The peak strength and stiffness of eroded soil are seen to decrease considerably as the number of seepage cycles increases. Multiple seepage-induced suffusion may create a collapsible soil structure in eroded soil, as shown by sudden decreases in deviator stress and stiffness, coupled by sharp increases in pore water pressure at small strain levels. As eroded soil might already be unstable, cyclic loading causes it to collapse, revealing a sudden increase in the generation of cyclic pore water pressure and a decrease in liquefaction resistance. The results highlight the importance of conducting laboratory tests to determine the impact of internal erosion on the strength and liquefaction resistance.
© 2021 Production and hosting by Elsevier B.V. on behalf of The Japanese Geotechnical Society. This is an open access article under the CC BY-NC-ND license (http://creativecommons.org/licenses/by-nc-nd/4.0/).

Keywords: Internal erosion; Suffusion; Laboratory tests; Hydraulic conductivity; Seepage

1. Introduction

Seepage-induced internal instability is one of the internal erosion mechanisms, described by the loss of the integrity of the soil by seepage flows, and is associated with the migration of the finer particles. Fannin and Slangen (2014) suggested that internal instability can be divided into two phenomena: suffosion and suffusion. *Suffosion* is the seepage-induced erosion of the finer particles with a reduction in the volume of the soil, since the coarser particles are floating within the finer matrix and are not in contact. *Suffusion* is the seepage-induced erosion of the finer particles from the skeleton of the coarser particles that are in contact; the finer particles are removed via the voids between the coarser particles by seepage flows, leaving the coarser skeleton intact. During suffusion, non-destructive volume deformation can be observed and the soil degrades due to the loosening structure caused by the loss of finer particles. Suffusion can alter the soil from a dense state to a loose state (Muir Wood et al., 2010) and can lead to a sudden collapse of the earthen structure due to the existence of unstable states within the eroded soil mass (Hicher, 2013). To understand the development of suffusion in a soil, the potential for soil suffusion has been studied using rigid-walled (Sherard et al., 1984; Kenney and Lau, 1985, 1986; Lafleur et al., 1989; Tanaka and Toyokuni, 1991;

Nomenclature

CSR	Cyclic stress ratio
D_r	Relative density
D_{rc}	Relative density after consolidation
D_{re}	Relative density after erosion
e_c	Global void ratio at end of consolidation or before erosion
e_e	Global void ratio after erosion
e_f	Inter-fines void ratio
e_i	Initial global void ratio after preparation
e_{max}	Maximum void ratio
e_{min}	Minimum void ratio
e_r	Global void ratio after reconsolidation
e_s	Inter-coarse void ratio
e_{se}	Inter-coarse void ratio after erosion
$e_{s,max}$	Maximum void ratio of coarse particles
FC	Initial fines content
FC_e	Fines content after erosion
FC^*	Critical fines content
i	Average hydraulic gradient
i_e	Average hydraulic gradient initiating erosion
k	Average hydraulic conductivity
k_i	Average initial hydraulic conductivity
k_e	Average end-of-test hydraulic conductivity
m_c	Initial mass of coarser fraction
m_e	Cumulative eroded mass loss
m_f	Initial mass of finer fraction
m_s	Initial mass of soil fraction
M_{ss}	Shear stress ratio at quasi-steady state

N	Number of cyclic loading cycles
N_s	Number of seepage cycles
$N_{ru=0.8}$	Number of cycle causing $r_u = 0.8$
p'	Mean effective stress
p'_i	Initial mean effective stress
p'_p	Mean effective stress at peak
p'_{ss}	Mean effective stress at quasi-steady state
p'_{pts}	Mean effective stress at phase transformation state
q	Deviator stress
q_p	Deviator stress at peak
q_{ss}	Deviator stress at quasi-steady state
r_u	Pore water pressure ratio
s_p	Initial peak strength
s_r	Residual strength
u	Pore water pressure
Δu	Excess pore water pressure
u_f	Flow potential
v	Discharge velocity
ε_a	Axial strain
ε_r	Average radial strain
ε_{af}	Axial strain at $r_u = 0.8$
ε_v	Volumetric stain at end of seepage test
σ'_a	Effective axial stress
σ'_r	Effective radial stress
ϕ_s	Angle of shearing resistance at quasi-steady state

Skempton and Brogan, 1994; Moffat and Fannin, 2006; Wan and Fell, 2008; Moffat et al., 2011; Ke and Takahashi, 2012; Sail et al., 2011; Nguyen et al., 2019) and flexible-walled (Bendahamane et al., 2008; Richards and Reddy, 2008; Marot et al., 2009; Chang and Zhang, 2011; Xiao and Shwiyhat, 2012; Ke and Takahashi, 2014a, 2014b; Ouyang and Takahashi, 2015; Slangen and Fannin, 2017; Mehdizadeh et al., 2017a, 2017b) permeameters. The rigid-walled permeameter has been widely used to perform erosion tests and to measure the local variations in density in one-dimensional downward or upward seepage flows. However, tests with the rigid-walled permeameter do not allow for an examination of the changes in stiffness and strength of eroded soils.

Fluctuations in the water level may affect the soil properties of potentially erodible earthen structures, such as cut-off walls, dams, and levees. To investigate the effect of a fluctuating water level on internal erosion, tests with multiple seepage flows may be needed. However, it is technically challenging to create multiple seepages in suffusion tests. Therefore, the suffusion tests reported in the literature have typically been performed under monotonic seep-

age flows (Bendahamane et al., 2008; Richards and Reddy, 2008; Marot et al., 2009; Chang and Zhang, 2011; Xiao and Shwiyhat, 2012; Ke and Takahashi, 2014a, 2015; Ouyang and Takahashi, 2015; Slangen and Fannin, 2017; Mehdizadeh et al., 2017a, 2017b). Understanding the long-term changes in the soil properties would be valuable for long-term stability assessments of potentially erodible earthen structures.

Although suffusion development has been widely investigated over the past decade, only limited studies have been able to experimentally examine the impact of suffusion on the soil mechanical responses. Several researchers have performed drained monotonic compression tests on post-suffusion soil (Chang and Zhang, 2011; Ke and Takahashi, 2014b, 2015). They found that initially dilative soil could turn contractive after the loss of substantial amounts of fine particles, and that the drained strength decreased after suffusion. Others have performed post-suffusion undrained triaxial compression tests on gap-graded soil (Xiao and Shwiyhat, 2012; Ke and Takahashi, 2014a; Ouyang and Takahashi, 2015; Mehdizadeh et al., 2017a, 2017b). Contrary to expecta-

tions, larger undrained shear strength and stiffness were observed in their tests. They reported that the soil became less contractive after suffusion. Ke and Takahashi (2014a) and Mehdizadeh et al. (2019) investigated the impact of suffusion on the undrained cyclic response of gap-graded soil. In their tests, the undrained cyclic resistance was found to be larger in the post-suffusion soil. This greater shear strength and cyclic resistance of eroded soil may be related to the coarser particle rearrangement accompanied by a reduction in volume, which is sometimes called suffosion (Fannin and Slangen, 2014). Studying the changes in a soil's microstructure after seepage through laboratory experiments is challenging (Nguyen et al., 2019), although these changes have been examined through numerical simulations (Yang et al., 2019a, 2019b, 2020). Thus far, experimental studies on the mechanical responses of post-suffusion soil have been discussed in the literature, but they are still not well understood. Further detailed testing will be crucial to an elaboration of the post-suffusion soil mechanical behaviour.

Although experimental research on internal erosion and its consequences is still in its infancy, these topics have been studied using numerical methods (Yang et al., 2019a, 2019b, 2020; Hu et al., 2020). For example, Yang et al. (2019a) investigated the clogging effect and heterogeneity caused by internal erosion using a probabilistic approach. They discovered that soil heterogeneity enhances the probability of clogging during the suffusion process by increasing the variability of the initial void distribution and fabric structure. Yang et al. (2020) studied the hydromechanical process of internal erosion and its impact on the mechanical response of gap-graded soil at different stress states, densities, and fines contents using numerical simulations. They found that the stress–strain behaviour of the soil changes from dilative to contractive after the loss of a large quantity of fine particles and with a decrease in shear resistance.

This paper presents an experimental investigation of suffusion under multiple seepage flows. The suffusion characteristics, in terms of the measurements of the fine particle loss, volume deformation, and hydraulic conductivity, are presented and discussed. The final section of this paper addresses the impact of suffusion on the undrained mechanical responses under monotonic and cyclic loading conditions. To the best of the authors' knowledge, suffusion tests on gap-graded soil with multiple seepages and post-suffusion compression tests with a pressure-controlled triaxial erosion device have seldom been performed. Consequently, the test results and their analysis given in this study will contribute to the knowledge of the internal erosion of soil and its impact on the mechanical behaviour, and will enhance risk and safety assessments of earthen structures, assisting in the prevention of internal erosion.

2. Laboratory experiments

2.1. Testing material

The gap-graded mixture of silica No. 3 and coloured silica No. 8 sands, with the same specific gravity of 2.645 but different particle sizes, is used as the test material. The particle shapes of silica sand No. 3, as the coarse fraction, and silica sand No. 8, as the erodible finer fraction, are categorised as sub-angular and angular, respectively, as discussed in Prasomsri and Takahashi (2020). The finer fraction refers to the fraction that can be eroded when studying internal erosion. It should be noted that silica sand No. 8 is regarded as the finer fraction in this study, although the particle size of this sand is larger than silt and clay-sized material (passing through Sieve No. 200 or 75 µm) according to the Unified Soil Classification System (ASTM D2487-11, 2012). A mixture with a fines content (percentage of mass ratio of silica sand No. 8 to the total mass of the soil specimen, FC) of 25% is used in this study. The initial fines content of 25% is selected as the finer fraction and is believed to offer a minor contribution to the coarser skeleton, as discussed in Prasomsri and Takahashi (2020). The particle size distributions of the two silica sands and the mixed specimen are presented in Fig. 1. The physical and gradation properties of the silica sands and the mixture are summarised in Table 1. The susceptibility of the mixture to internal instability is assessed by the Kézdi (1979) and Kenney and Lau (1986) criteria. The results of the assessment are summarised in Table 2 and indicate that the mixture is potentially unstable.

2.2. Testing apparatus

The modified triaxial erosion apparatus at the soil mechanics laboratory of the Department of Civil and Environmental Engineering, Tokyo Institute of Technology, is used to perform the tests. A schematic diagram of the over-
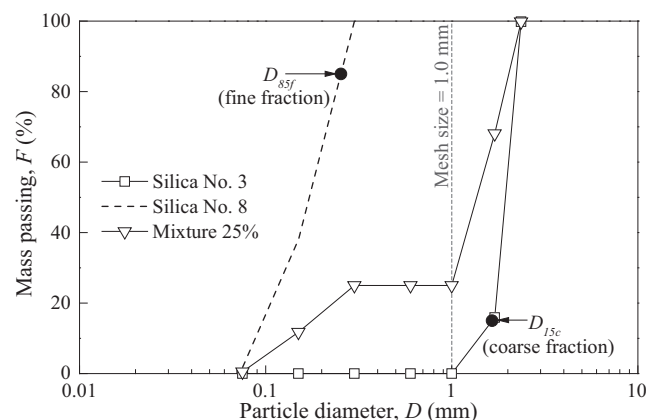

Fig. 1. Particle size distribution curves of soils.

Table 1
Physical and gradation properties of test materials.

Physical and grading properties	Silica No. 3	Silica No. 8	25% Mixture
Specific gravity, G_s	2.645	2.645	2.645
Maximum void ratio, e_{max}	0.98	1.24	0.73
Minimum void ratio, e_{min}	0.75	0.88	0.44
Uniformity coefficient, C_u	1.47	2.18	11.41
Curvature coefficient, C_c	1.60	0.98	5.35
D_{15c} (mm)[a]	1.65	–	1.65
D_{85f} (mm)[b]	–	0.25	0.25
$(H/F)_{min}$[c]	–	–	0.62
Soil classification, $USCS$[d]	SP	SP	SM
Particle description	Sub-angular ∼ Angular		

Note:
[a] D_{15c} is the particle diameter in which 15% by mass of coarse particles passed.
[b] D_{85f} is the particle diameter in which 85% by mass of fine particles passed.
[c] F is the passed fraction by mass finer than d, and H is the mass fraction between d and $4d$ (Kenney and Lau 1985, 1986).
[d] The mixture is classified as silty sand (SM) regarding Silica No. 8 as finer fraction.

all layout is shown in Fig. 2. The apparatus comprises an automated triaxial system, modified seepage control system, and eroded soil collection unit. One of the key features of the modified triaxial erosion apparatus is that it can be used for internal erosion experiments with high back pressure under pressure-controlled multiple seepage conditions. Detailed information on this apparatus is given in Prasomsri and Takahashi (2020).

2.3. Testing procedure

The specimens are prepared by the moist tamping method introduced by Ladd (1978) with an initial moisture content of 10% to avoid the segregation of the two different particle sizes. The nonlinear average under-compaction criterion, proposed by Jiang et al. (2003), is adopted to produce uniform soil specimens. The dimensions of the cylinder samples are 150 mm in height and 75 mm in diameter. Back pressure of 400 kPa (for 10 h) is applied to ensure complete saturation. By doing so, a B-value of greater than 0.95 is typically achieved. The specimens are then isotopically consolidated to obtain the mean effective

Table 2
Summary of assessment results of internal instability.

References	Geometric criteria: internally unstable if	25% Mixture
Kézdi (1979)	$(D_{15c}/D_{85f})_{max} \geq 4$	U
Kenney and Lau (1986)	$(H/F)_{min} \leq 1.0$	U

Note: U is unstable, S is stable

stress (p'_i) of 50 kPa. During consolidation and reconsolidation, the changes in void ratio are derived from the changes in volume calculated by measuring the amounts of water flowing in and out of the specimens through a burette and a differential pressure transducer.

Seepage testing is performed at the same stress state after isotropic consolidation. The seepage in this investigation is under isotropic stress, but the seepage in the field is most likely to be under anisotropic stress. However, as the specimens in this study are only seen as a small element of the earthen structure, the tests are performed under isotropic conditions for simplicity. The specimen with erosion named "WE_N1" is subjected to one seepage cycle. To impose the seepage, the pressure near the inlet tank (ITP) is automatically increased from 400 to 430 kPa at increments of 2 kPa/min, while the pressure at the base of the specimen (BP) is automatically maintained at 400 kPa. Thus, unidirectional downward seepage flow can be imposed through the specimen, while maintaining the applied back pressure. The ITP is kept constant at 430 kPa for about 20 min and then decreased to 400 kPa at the same increments. The pressure transducer is used to measure the pore water pressure at the top of the specimen (TP). It is noted that the difference between the TP and the ITP is the head loss in the fittings and the tubes. The top and base pore water pressures are represented by TP and BP, which are closely connected to the top and base of the specimen, respectively. With this system, both the flow rate and the differential pore water pressure change during the seepage testing. The same seepage shape is created for two more specimens with erosion, "WE_N3" and "WE_N5", with three and five cycles, respectively. The designation of "R" is used when a test is repeated. Throughout each seepage test, zero-deviator stress is maintained automatically, allowing the specimen to experience seepage flow under isotropic stress conditions. The axial and radial displacements, pore water pressure, deviator stress, flow rate, and cumulative eroded soil mass are continuously recorded. The discharge velocity (v) is derived from the flow rate and the cross section of the current specimen. The average hydraulic gradient (i) is calculated using the differential pressure between the TP and the BP and the length of the current specimen. The average saturated hydraulic conductivity (k) is calculated according to Darcy's law. The volumetric strain (ε_v) is estimated based on the right cylinder assumption, which can be determined from the combination of the axial strain and average radial strain measured by clip gauges. The eroded soil mass (m_e) comprises the eroded fine particles measured at the measuring tray. After the suffusion test, a B-value of greater than 0.95 is still attained due to the continuation of high back pressure on the tested specimens during the seepage testing. The testing program and its major parameters are summarised in Table 3.

In the undrained shearing stage, strain-controlled compression with the axial strain rate of 0.1%/min is performed. Corrections for the changes in the cross-sectional
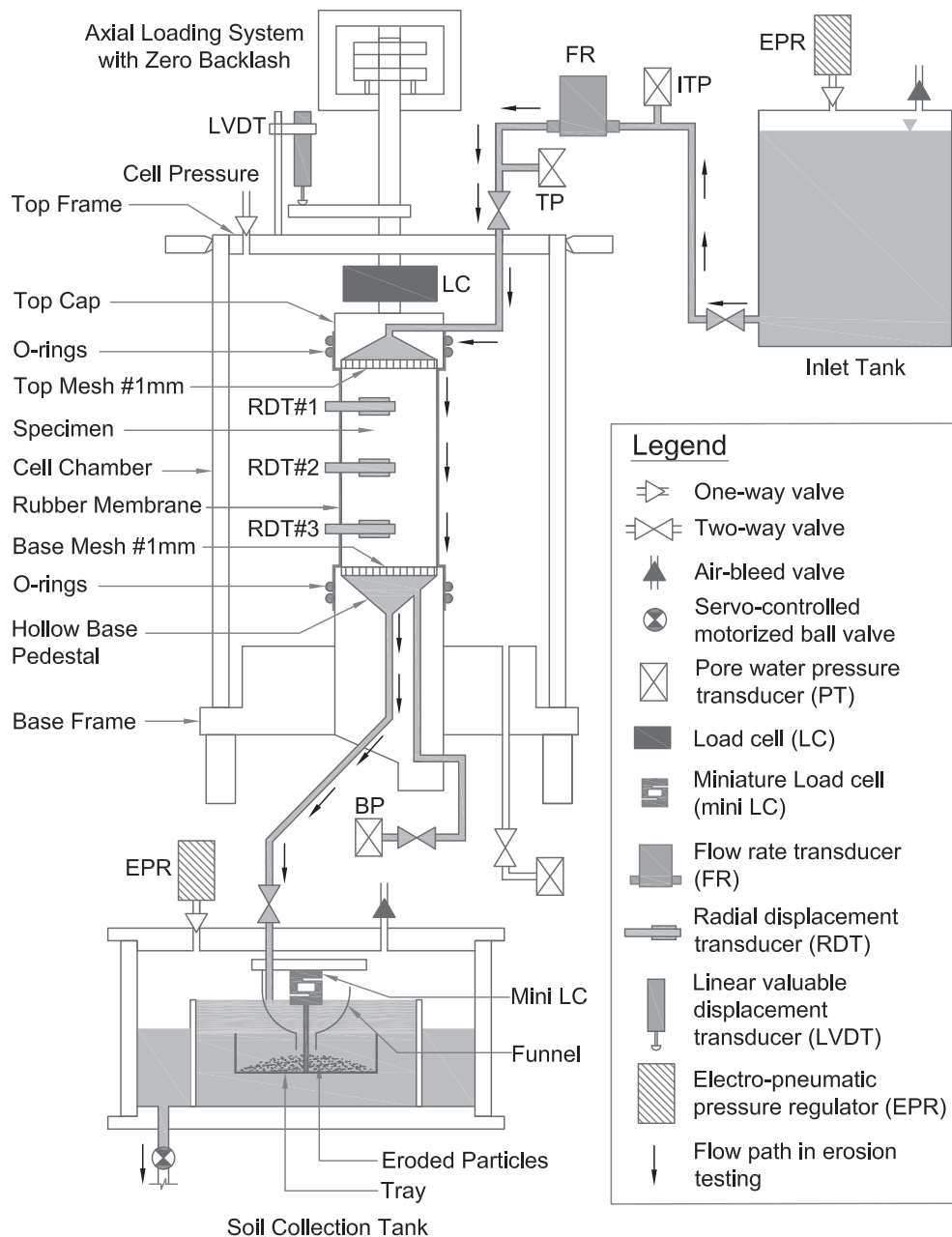
Fig. 2. Schematic diagram of modified triaxial erosion apparatus.

area and membrane penetration during shearing are carried out. The multistage undrained cyclic shearing tests are conducted on the specimens with the "C" test code. The two-way loading of compression and extension with an axial strain rate of 0.25%/min is applied until the pore water pressure ratio ($r_u = \Delta u/p'_i$) reaches 0.8, which is defined as the cyclic resistance criterion for this study in order to minimise the collapse of the soil structure. The soil structure begins to break down when $r_u = 1.0$ (Mitchell and Soga, 2005). The cyclic stress ratios ($CSR = q/2p'_i$) of 0.10, 0.15, and 0.20 are applied. After each cyclic shearing, the specimen is isotropically reconsolidated at $p' = 50$ kPa. The relationship between the applied CSR and $N_{ru=0.8}$

(number of cyclic shearings to reach $r_u = 0.8$) is expressed graphically as a cyclic resistance curve. Inevitably, the multistage cyclic shearing with reconsolidation produces cumulative increases in the cyclic resistance due to densification (Ishihara and Okada, 1982; Towhata and Ishihara, 1985; Bouferra et al., 2007). It may be disputed that the proposed cyclic resistance curves are be impractical. However, it is thought that the same distribution of the surviving finer fraction along the eroded specimen could not be obtained with different suffusion testing due to unavoidable non-uniformities of seepage flow. Multistage cyclic shearing with reconsolidation could allow for the observation of the cyclic responses of the same eroded specimen under dif-

Table 3
Summary of major parameters in the tests.

Test code	Initial conditions					Initiation and end-of-test conditions								
	B-value	e_c	e_s	D_{rc} (%)	k_i (m/s)	N_s	i_e	m_e (g)	ε_v (%)	FC_e (%)	e_e	e_{se}	D_{re} (%)	k_e [a] (m/s)
WOE	0.99	0.58	1.10	53	–	–	–	–	–	–	–	–	–	–
WOE_R	0.99	0.58	1.10	54	–	–	–	–	–	–	–	–	–	–
WE_N1	0.96	0.58	1.10	54	4.2E-04	1	0.9	11.1	0.01	24.2	0.59	1.10	49	6.0E-04
WE_N1_R	0.96	0.57	1.10	56	4.6E-04	1	1.2	7.4	0.01	24.5	0.58	1.10	52	4.7E-04
WE_N3	0.97	0.57	1.10	55	6.9E-04	3	0.6	24.7	0.03	23.3	0.61	1.10	42	7.7E-04
WE_N5	0.97	0.57	1.09	56	6.1E-04	5	0.5	35.4	0.06	22.5	0.62	1.09	38	8.2E-04
WOE_C	0.98	0.57	1.10	54	–	–	–	–	–	–	–	–	–	–
WE_N3_C	0.97	0.57	1.10	55	5.1E-04	3	0.8	16.4	0.01	23.9	0.60	1.10	47	7.0E-04
WE_N5_C	0.98	0.57	1.10	55	6.7 E-04	5	0.7	30.5	0.04	22.9	0.62	1.10	40	9.4E-04

Test code	Microstructure case[b]	Microstructure description[c]	Change in k after initiation of erosion[d]	Marked volume change[e]	Internal instability phenomenon[f]
WOE	iii	UF	–	–	–
WOE_R	iii	UF	–	–	–
WE_N1	iii	UF	↓↑	No	SF→SU
WE_N1_R	iii	UF	↓↑	No	SF→SU
WE_N3	iii	UF	↓↑	No	SF→SU
WE_N5	iii	UF	↓↑	No	SF→SU
WOE_C	iii	UF	–	–	–
WE_N3_C	iii	UF	↓↑	No	SF→SU
WE_N5_C	iii	UF	↓↑	No	SF→SU

Note:
[a] k_e is the hydraulic conductivity at the end of constant head period of the last seepage cycle.
[b] Microstructure case is referred to Thevanayagam and Mohan (2000).
[c] UF is underfilled microstructure.
[d] ↓ is decrease; ↑ is increase.
[e] Volume change is negligible; if $e_v \leq 0.06\%$ (accuracy of volume measurement).
[f] SF is self-filtering; SU is suffusion.

ferent cyclic loading magnitudes because the distribution of the surviving finer fraction along the eroded specimen would remain constant.

3. Seepage test results and data interpretation

A total of six seepage tests are performed on medium dense sand specimens with an initial relative density (D_r) of 50% at p'_i of 50 kPa. The test results are summarised in Table 3. The variation in finer fractions for each test, caused by internal erosion, is summarised in Table 4. In the following, the seepage test results for WE_N3 are presented as an example. In this case, the specimen is subjected to three seepage cycles. The changes in *ITP*, *TP*, *BP*, *i*, m_e, ε_v, *v*, and *k* with elapsed time are plotted in Fig. 3. The results of the seepage tests are interpreted according to three aspects: 1) hydraulic response, 2) erosion characterisation, and 3) visual observation and post-test particle size distribution.

3.1. Hydraulic response

The variations in *ITP*, *BP, TP*, and *i* with elapsed time for WE_N3 are plotted in Fig. 3a. When *ITP* increases in Cycle 1, *i* increases correspondingly. Meanwhile, a noticeable migration of the finer fraction is detected. The hydraulic gradient required to initiate internal erosion (i_e), which

is determined by the first detection of m_e, is 0.6 in this case, as indicated by the star symbol in Fig. 3a. When *ITP* remains constant, a gradual decrease in *i* is observed. *i* gradually decreases in Cycle 2 and becomes constant in Cycle 3. The decrease in hydraulic gradient with the number of seepage cycles (N_s) is likely to be caused by the washout of fine particles from the specimen.

The variations in *v* and *k* with elapsed time for WE_N3 are shown in Fig. 3b. The variation in *k* is derived from the relationship between *i* and *v*. The response of *k* could explain the development of the suffusion phenomenon. The response can be divided into two stages, namely, before and after the initiation of erosion. Before the initiation of erosion, the initial hydraulic conductivity (k_i) value is approximately constant at $k_i = 6.9 \times 10^{-4}$ m/s. After the initiation of erosion in Cycle 1, *k* first decreases and subsequently increases. In a continuous head period of Cycle 2, *k* gradually increases and becomes approximately constant in Cycle 3. The end-of-test hydraulic conductivity (k_e) is the value of *k* in the constant head period before the descending seepage flow in the last seepage cycle, namely, $k_e = 7.7 \times 10^{-4}$ m/s in this case. It should be noted that *k* fluctuates widely in the seepage flow, descending and ascending in the subsequent cycles. Thus, the change in *k* in this period is not analysed. The fluctuation in hydraulic conductivity is caused by the variations in the hydraulic gradient and discharge velocity during the descending and ascending of the

seepage flow. The descending and ascending seepages may create a reversal of the seepage force, which can increase the finer particle mobility in the specimen, resulting in the continued detaching and clogging of the finer particles locally. The average hydraulic conductivity might easily fluctuate with changes in the local hydraulic conductivity determined by the local detaching or clogging of the finer fraction. The local detaching or clogging of the finer fraction is dependent on the heterogeneous soil microstructure along the specimen.

The decrease in hydraulic conductivity suggests that some detached particles cause the clogging of the pore throat within the specimen. As the seepage velocity increases, it can unclog these particles, leading to the subsequent increase in k observed in Cycle 1. Similar phenomena were also observed in the gap-graded soil with an initial fines content of 25% by Rochim et al. (2017) and Zhong et al. (2018), indicating the combination of detachment, transport, and filtration of the finer particles during the seepage-induced erosion.

Interestingly, in Fig. 3, k decreases even if i and v increase before $t = 13.0$ min. This response is attributed to the relocation and erosion of the finer particles induced by seepage flow. As the finer particles near the bottom can be easily washed out, an eroded soil mass is detected. However, during this period, the clogging has already started at a certain location other than the bottom of the specimen. As the pore water pressure at the top of the specimen monotonically increases with time during this period, more finer particles are trapped in the clogging zone because of the excessive supply of finer particles from the upper portion of the specimen. After $t = 13.0$ min, k increases with the decreasing i and the slightly increasing v, whereas m_e increases slightly before becoming constant. This response is likely to be due to a decrease in the detached finer particle supply from the upper portion of the specimen and the gradual migration of finer particles from the clogged zone, resulting in a decrease in water flow resistance and an increase in hydraulic conductivity.

The gradual increase in k before converging to a constant value in subsequent cycles suggests that, with the progress of suffusion, the dislodgement of fine particles increases the size and number of localised internal erosion channels in the specimen, leading to an increase in

hydraulic conductivity. The erosion of fine particles causes the length of the flow path to decrease with seepage cycles and creates preferential flow paths leading to a steady state in the last cycle.

The evolution of k for all eroded specimens is illustrated in Fig. 4a. It is found that a similar evolution of k is observed for all specimens. k firstly decreases, subsequently increases in Cycles 1 and 2, and stabilises after Cycle 3. The temporal diminishing k confirms the complex suffusion phenomenon that appears as a combination of the detachment, transport, and clogging of fine particles, as discussed by Rochim et al. (2017) and Zhong et al. (2018). The stabilisation of k after Cycle 3 can be explained by the incident of preferential flow paths induced by the multiple suffusion processes.

The value of i_e for all eroded specimens is summarised in Table 3, indicating that the erosion of fine particles occurs at a relatively small hydraulic gradient of about 0.5–1.2. The small value of i_e is attributed to the fine particles being confined and unstressed within the voids between the coarse particles (Skempton and Brogan, 1994; Shire et al., 2014). Some fine particles can be eroded out at a small hydraulic gradient as they are not connected to any force chains, while coarse particles are mainly in contact and dominate the force chains. It should be noted that the detection of suffusion initiation is based on the measurement of the eroded mass at the measuring tray. The eroded mass is measured later in comparison to the flow rate of interstitial pressure. The corresponding delay may induce a discrepancy in the determination of i_e.

3.2. Erosion characterisation

The evolution of the m_e of WE_N3 in Fig. 3c indicates that the fine particles are eroded from the specimen with N_s. Typically, the m_e in each cycle increases rapidly in the early stage of seepage, but it ceases to increase over time, and finally converges to a constant value by the end of the cycle. This tendency is consistent with the results obtained in the relevant studies (Ke and Takahashi, 2014a, 2014b; Ouyang and Takahashi, 2015; Jiang and Soga, 2017). It is worth noting that the change in m_e in one cycle is not monotonic. Approximately 12.2 g, 4.3 g, and 8.2 g of the finer fraction are lost in Cycles 1, 2, and

Table 4
Variation of finer fraction in seepage tests.

Test code	Before erosion			After erosion			
	Coarser fraction, m_c (g)	Finer fraction, m_f (g)	Fines content, FC (%)	Eroded fines, m_e (g)	Survived fines, $m_f - m_e$ (g)	Fines content after erosion, FC_e (%)	Eroded percentage, m_e/m_f (%)
WE_N1	829.7	276.6	25.0	11.1	265.4	24.2	4.0
WE_N1_R	829.7	276.6	25.0	7.4	269.2	24.5	2.7
WE_N3	829.7	276.6	25.0	24.7	251.9	23.3	8.9
WE_N5	829.7	276.6	25.0	35.4	241.2	22.5	12.8
WE_N3_C	829.7	276.6	25.0	16.4	260.2	23.9	5.9
WE_N5_C	829.7	276.6	25.0	30.5	246.1	22.9	11.0

3, respectively. The erosion of fine particles forms preferential flow paths in Cycle 1. Subsequently, some of the detached fine particles are trapped within the specimen itself in Cycle 2, resulting in smaller eroded fine particles. Once Cycle 3 is performed, the filtered particles can be washed away, which is coincidental with the larger amount of loss of fine particles. The imposed cyclic seepage flow is sufficient for restricting the clogging process and force erosion of the fine particles.

The preferential flow paths can be generated longitudinally throughout the specimen by the erosion of the finer fraction, according to the microstructural experimental study by Nguyen et al. (2019). The mechanics of erosion and clogging can be investigated using the coupled computational fluid dynamics and discrete element method (CFD-DEM) (Hu et al., 2020; Xiong et al., 2021a, 2021b). CFD-DEM analyses have shown that the fine particles can be transported in some way through a specimen before eventually clogging the pores; the greater the distance that the fine particles are transported, the more likely they are to get clogged. Numerical analysis has shown that clogging is due to the polydisperse nature of the void constriction sizes, which is dependent on the gradation curve, density, and particle shape (Shire and O'Sullivan, 2016).

The loss of fine particles increases from 4.3 g to 8.2 g from Cycle 2 to Cycle 3, while the hydraulic gradient slightly decreases during these cycles and is accompanied by an increase in discharge velocity. The results suggest that the suffusion process can induce the local clogging of the detached particles accompanied by variations in the discharge velocity and hydraulic gradient. Therefore, the combination of the pressure gradient and the discharge velocity is necessary for evaluating the hydraulic loading history, as suggested by Reddi et al. (2000) and Marot et al. (2016).

Regarding the evolution of ε_v in Fig. 3c, it is apparent that no marked change in ε_v can be observed during the test period for any of the specimens, whereas the eroded soil mass and hydraulic conductivity continue to increase. This suggests that there is no significant redisposition of the coarse particles. Therefore, the loss of fine particles should directly result in an increase in voids among the coarse particles. The evolution of ε_v for all eroded specimens is shown in Fig. 4b. It is found that the eroded specimens show a slightly larger ε_v at a larger number of imposed seepages (e.g., WE_N5 and WE_N5_C). At the end of the test, however, ε_v ranges from about 0.01–0.06%, which is close to the ±0.06% accuracy of the volumetric strain measurement and is considered to be a negligible change in volume. Based on the evolution of the eroded mass, hydraulic conductivity, and volumetric strain, the seepage responses of these tests can be characterised by the first constant hydraulic conductivity followed by a sequence of decreases and increases in hydraulic conductivity, without any marked change in volumetric strain and with the migration of fine particles. These responses are termed self-filtering and they are followed by suffusion.

The evaluation of m_e for all eroded specimens is illustrated in Fig. 4b, indicating that a greater number of imposed seepage cycles induces a larger cumulative eroded mass. The cumulative eroded mass seems to reach an asymptote, but the hydraulic conductivity increases at the end of Cycles 1 and 2. The stabilisation of hydraulic conductivity is observed at the end of Cycles 3, 4, and 5. These results suggest that a greater number of seepage cycles could lead to the end of the suffusion process. Rochim et al. (2017) suggested that the end of the suffusion process can be defined as the stabilisation of both the hydraulic conductivity and the erosion rate. Therefore, the number of hydraulic loadings has a significant influence on the hydraulic behaviour of specimens and the development of suffusion.

Moreover, the cyclic seepage flow characteristics (i.e., rising and falling rates of the seepage flow velocity and duration of the seepage stage) could also consistently influence the seepage test results, and thus, require further investigation. The effect of the hydraulic loading history was observed by Luo et al. (2013) and Rochim et al. (2017). For example, Luo et al. (2013) performed erosion tests with two test durations and concluded that a long-term large hydraulic head increases the eroded mass dramatically. Rochim et al. (2017) found that, depending on the hydraulic loading history, suffusion development can involve either clogging or erosion, and that applying a higher rate of rising in the seepage flow velocity can limit the clogging process.

The seepage test results indicate that a loss of the eroded mass, volumetric strain, and a change in hydraulic conductivity occur simultaneously and are fully combined. These parameters are necessary for describing the internal erosion mechanism, which has been captured reasonably well through the modified triaxial erosion apparatus.

The seepage test repeatability in this study is validated by comparing the time records of the eroded soil mass, volumetric strain, and hydraulic conductivity, especially in the two tests on WE_N1 and WE_N1_R, shown in Fig. 4. Most of the variations are reasonably consistent, which implies good repeatability of the seepage tests, although some minor differences in hydraulic conductivity are evident.

3.3. Visual observation and post-test particle size distribution

A digital microscopic image of specimen WE_N5_C is shown in Fig. 5, capturing the top surface of the specimen after its preparation. The image is utilised as additional evidence when discussing the contacts between the particles of the mixtures. It is seen that most of the coarse particles are mainly in contact with each other, while the fine particles seem to occupy some locations between the coarse particles. This suggests that the fine particles would be confined and unstressed within the voids between the coarse particles and transported by seepage flows.
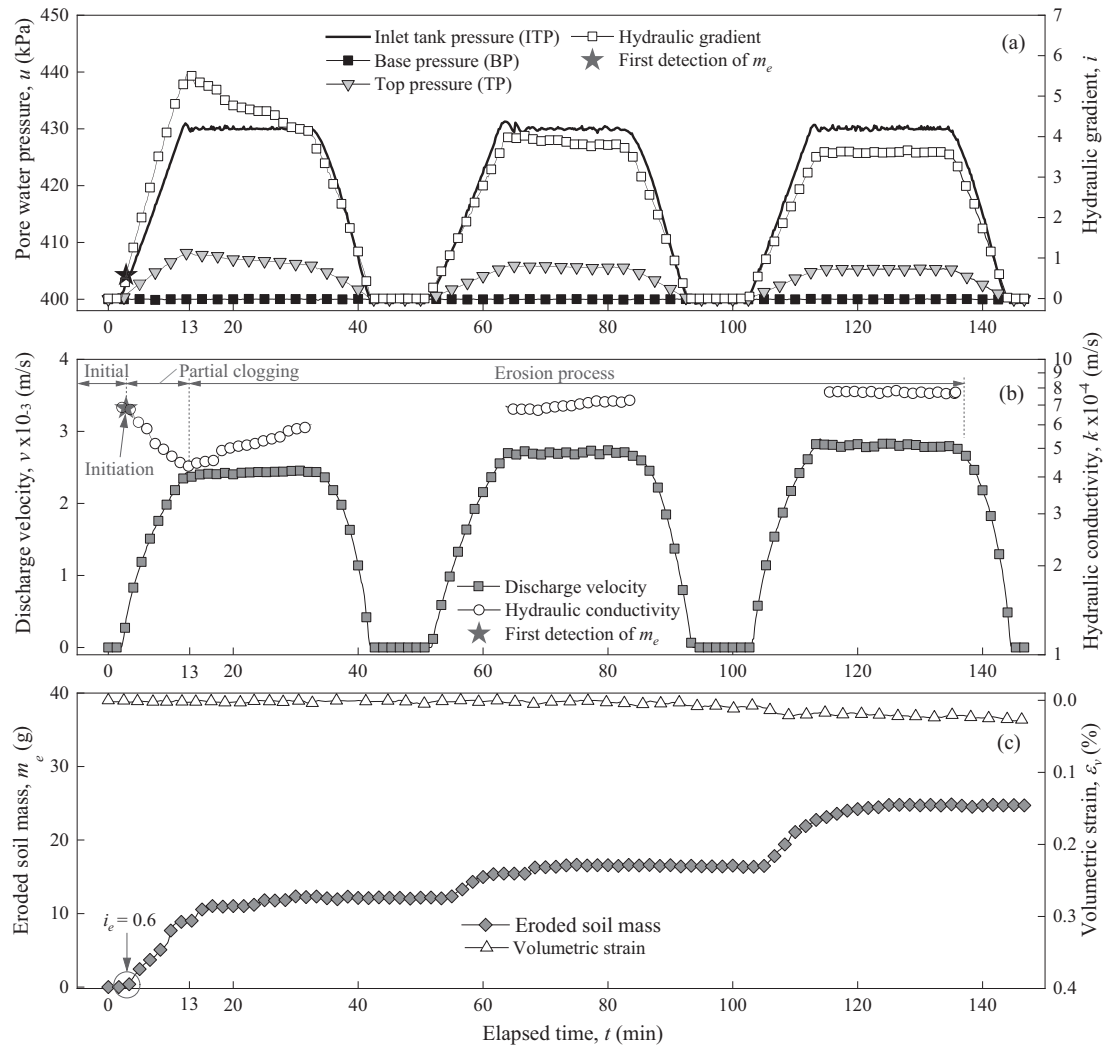
Fig. 3. Typical seepage test results: time histories of (a) pore water pressures and hydraulic gradient, (b) discharge velocity and hydraulic conductivity, and (c) eroded soil mass and volumetric strain for WE_N3.

At the end of the test, photographs are taken of the cross section of specimen WE_N5_C at a different depth from the top to observe the spatial distribution of the surviving fine particles, as shown in Fig. 6. The localised channels are observed throughout the specimen length. Few fine particles appear on the top surface; the accumulation of fine particles is greater in the middle and base parts. This suggests that the erosion of fine particles is more critical in the top part of the specimen and induces the heterogeneity of the specimen. The concentrated channels appear inside and near the side along the depths of the specimen, indicating the randomness of the suffusion development. Each specimen is divided into three parts, and the post-test particle size distribution is measured. Fig. 7 presents the initial gradation and the post-test gradations of the top, middle, and base parts of the specimen corresponding to depths of 0–5 cm, 5–10 cm, and 10–15 cm, respectively, from the top. The loss of fine particles is greatest in the top part. These results agree with previous investigations (*e.g.*, Ke and Takahashi, 2014a, 2014b; Ouyang and

Takahashi, 2015; Rochim et al. 2017). Moreover, because of the accumulation of fine particles in the base part, the finer fraction is slightly larger than the initial gradation; and thus, local clogging is likely to occur around the base part of the specimen.

4. Soil microstructure and densification state after suffusion

Thevanayagam and Mohan (2000) proposed an intergranular matrix phase diagram, expressed in terms of the fines content and global, inter-coarse, and inter-fines void ratios, to explain the interaction of the coarse and fine particles in a soil microstructure and the densification state of gap-graded soil. Following that, Yin et al. (2016) developed a unified void ratio index for gap-graded soil to model the finer particle effect on the mixture microstructure packing and undrained mechanical behaviour of sand-silt mixtures. Fig. 8 illustrates the intergranular matrix phase diagram constructed in this study. The minimum and maximum void ratios (e_{min} and e_{max}), determined by the procedures
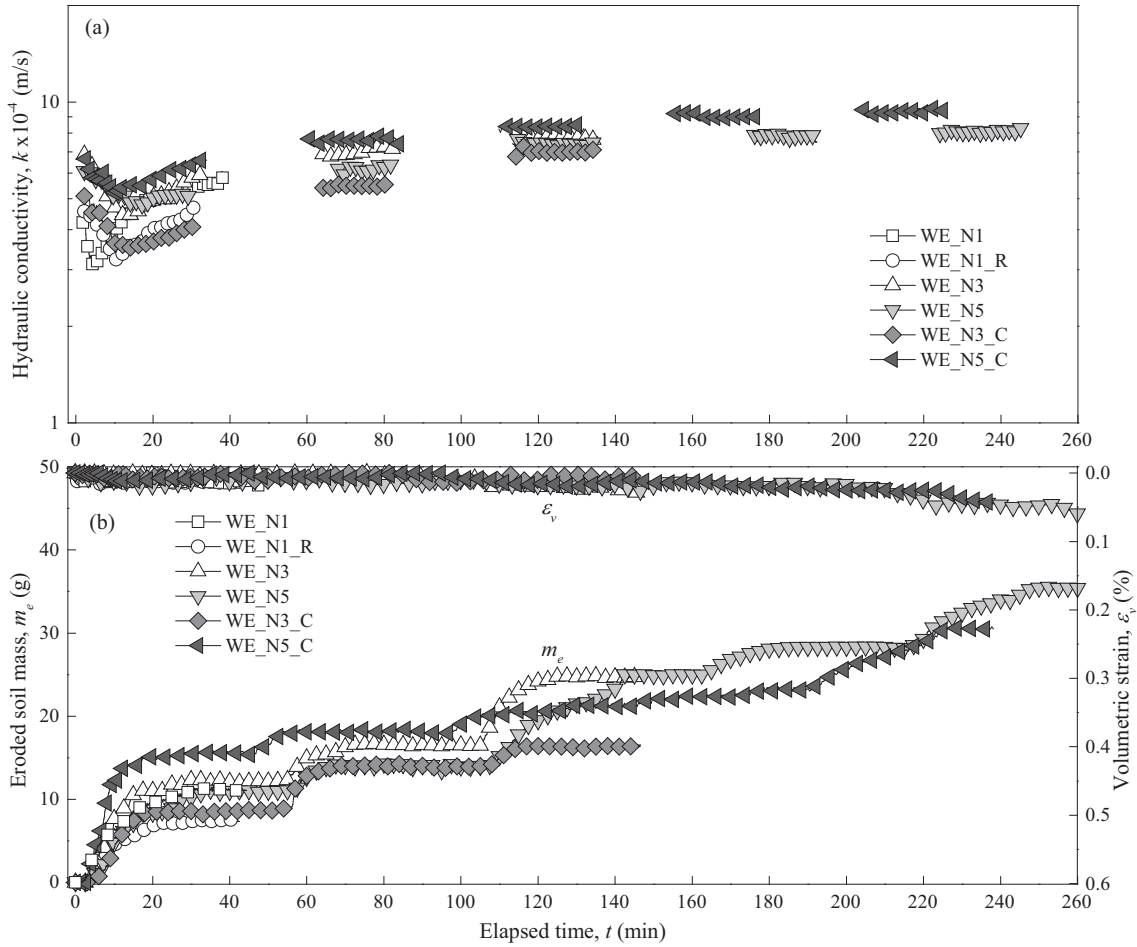
Fig. 4. Time histories of (a) hydraulic conductivity and (b) eroded soil mass and volumetric strain for all eroded specimens.

proposed by Lade et al. (1998), are plotted in the figure. Here, the trends of e_{min} and e_{max} are considered as the densest and loosest states of the mixtures, respectively. The solid lines on the left-hand side represent the inter-coarse void ratio of the mixture (e_s) and are expressed by

$$e_s = \frac{e + FC}{1 - FC} \tag{1}$$

where e is the global void ratio and FC is the fines content. It should be noted that the fines content by mass is the same as that by volume since the specific gravity of all the particles is the same. In this study, FC is also used for the fines content by volume. The dashed lines on the right-hand side represent the inter-fines void ratios of the mixture (e_f) and are expressed by

$$e_f = \frac{e}{FC} \tag{2}$$

The area sandwiched by these four lines is neither coarse-controlled nor fine-controlled. The transitional fines content is thought to be approximately 28.4–30.5%, which is indicated by the intersections between e_s and e_f. For the

experimental results, e_{max} and e_{min} are likely reach a minimum value at an FC of about 30%, considered as the critical fines content (FC^*) based on Yang et al. (2006b).

According to Thevanayagam and Mohan (2000), the intergranular matrix phase can be categorised into four cases. In Cases 1 through 3, $FC < FC^*$, and the soil has an "underfilled" microstructure. In Case 1, $e < e_{s,max}$ (maximum void ratio of the coarse particles), and the coarse particles are in contact with each other and control the soil behaviour. In Case 2, $e \approx e_{s,max}$, and the fine particles sit inside the voids between the coarse particles. In Case 3, $e > e_{s,max}$, and most of the coarse particles are separated by fine particles; the fine particles can be eroded out if a large enough seepage force is applied. In Case 4, as $FC > FC^*$, an "overfilled" microstructure is generated, and most of the coarse particles are floating in the fine matrix and the fine particles control the soil behaviour.

The microstructure and densification state for each test are evaluated by plotting the initial FC against the void ratio after consolidation (e_c) for the non-eroded specimens and the fines content after erosion (FC_e) against the void ratio after erosion (e_e) for the eroded specimens on the diagram shown in Fig. 8. The change in e_e is calculated using

the method proposed by Scholtès et al. (2010), in which the eroded mass loss and volume change are considered, as expressed by Eq. (3). The FC_e is calculated by Eq. (4). e_c is smaller than the initial global void ratio after the preparation (e_i), leading to the relative density before erosion (D_{rc}) being larger than the relative density after the preparation (D_r), as listed in Table 3. The relative density after erosion (D_{re}) is estimated by Eq. (7).

$$e_e = (1 - \varepsilon_v)\left(\frac{e_c + m_e/m_s}{1 - m_e/m_s}\right) - \varepsilon_v \tag{3}$$

$$FC_e = \frac{m_f - m_e}{m_f - m_e + m_c} \tag{4}$$

$$D_r = \frac{e_{max} - e_i}{e_{max} - e_{min}} \tag{5}$$

$$D_{rc} = \frac{e_{max} - e_c}{e_{max} - e_{min}} \tag{6}$$

$$D_{re} = \frac{e_{max} - e_e}{e_{max} - e_{min}} \tag{7}$$

where m_s is the initial soil mass, including the finer and coarser fractions (m_f and m_c), and ε_v is the volumetric strain at the end of the seepage test.

The soil state in the intergranular matrix phase in Fig. 8 and the supplemental micro-observation in Fig. 5 suggest that the microstructure of these specimens in Case 3 is categorised as underfilled; it is coarse-dominated with a partial fine-supported microstructure. After the specimens experience the multiple seepage flows, e_e increases with N_s, resulting in a diminishing relative density. It can be seen in Fig. 8 that the trend of the soil densification state after erosion or $e_e - FC_e$ moves toward the loosest state line. The inter-coarse void ratios after erosion (e_{se}) for all the tested specimens are calculated from Eq. (8) and listed in Table 3. It is observed that e_s and e_{se} are the same for all specimens, indicating that a decrease in the volume of fine particles is directly replaced by the voids among the coarse particles. This suggests that the voids among the coarse particles would become larger; thus, the major structure formed by the coarse particles would be more unstable. Consequently, the increase in e_e and constant e_{se} with the decrease in FC_e would significantly affect the undrained responses in the triaxial compression tests.

$$e_{se} = \frac{e_e + FC_e}{1 - FC_e} \tag{8}$$

5. Undrained mechanical responses in triaxial compression

5.1. Undrained monotonic response

5.1.1. Stress–strain behaviour and pore water pressure response

The stress–strain curves or deviator stress (q) versus axial strain (ε_a), pore water pressure (u) responses, and the effective stress paths or deviator stress (q) versus mean effective stress (p') for the undrained compression tests on the non-eroded and eroded specimens are shown in Fig. 9

($q = [\sigma'_a - \sigma'_r]/2$ and $p' = [\sigma'_a + 2\sigma'_r]/3$, where σ'_a is the effective axial stress and σ'_r is the effective radial stress). A summary of the test results is presented in Table 5.

The results for the non-eroded specimens, WOE and WOE_R, in the stress–strain space, show the peak deviator stress followed by strain softening. The deviator stress starts increasing again with straining due to dilative behaviour after passing through the phase transformation point, which can be defined as a contractive-dilative response. The repeatability of the undrained monotonic shearing can be validated by comparing the stress–strain curves, pore water pressure responses, and stress paths between WOE and WOE_R in Fig. 9. The results for these two specimens exhibit good repeatability.

The eroded specimens show smaller peak strength, a larger degree of strain softening, and greater contractive responses than the non-eroded specimens. The peak strengths for all the eroded specimens are smaller at a larger number of seepage cycles, whereas the deviator stress at large strain is almost the same regardless of the number of seepages. As can be seen in Fig. 9**a and b**, there is a sharp drop in deviator stress corresponding to a sharp increase in the pore water pressure response at the axial strain of 11.5% observed in specimen WE_N3. The drop in deviator stress is also observed in specimen WE_N1_R at the axial strain of 8.5%. The authors postulate that the drops in deviator stress are a result of the collapse of the unstable skeleton of the coarse particles caused by the erosion of the fine particles.

The development of pore water pressure in the eroded and non-eroded specimens with the phase transformation points (Ishihara et al., 1975) is illustrated in Fig. 9**b**. In the non-eroded specimens, the pore water pressure develops as the nonlinear response at small strains, rapidly increasing with further straining to reach the peak at medium strain, and gradually decreasing after passing through the phase transformation point. The pore water pressure increases faster at the small stain in the eroded specimens, reaches a larger peak at medium strain, and stays constant through the phase transformation state. The maximum

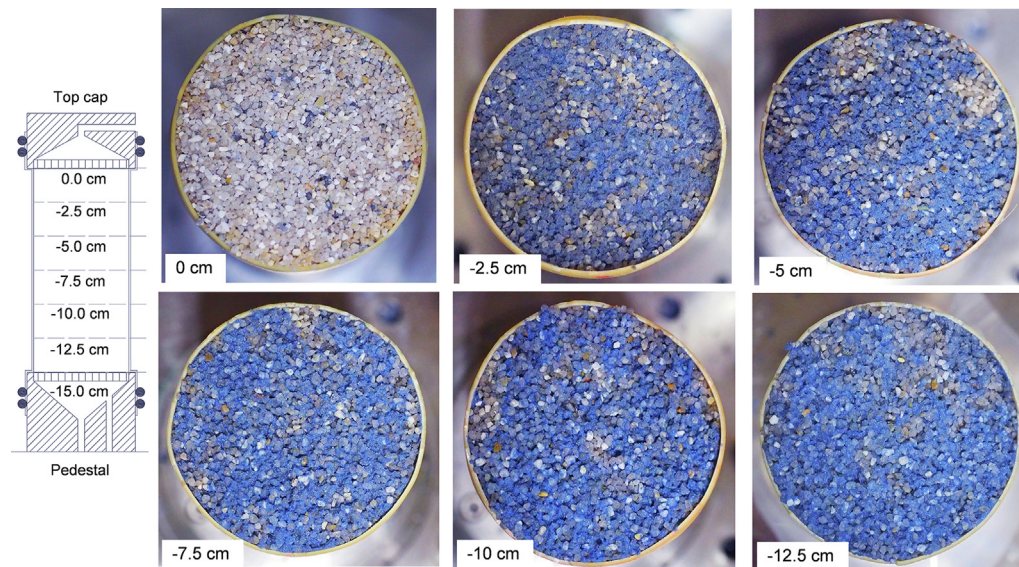Fig. 5. Microscope image after specimen preparation for WE_N5_C.

Fig. 6. Photographs of cross section of specimen at different depths from top for WE_N5_C.

pore water pressure maintains almost the same value irrespective of the changes in void ratio and fine particle loss. The authors believe that the initial nonlinear pore water pressure response could be linked to the soil microstructure. The medium dense sand mixture with $FC < FC*$ would have an underfilled microstructure in which the fine particles are confined within the voids between the coarse particles, where most of the coarse particles are in contact with each other (Shire et al., 2014). Better interlocking between the coarse particles would produce the temporal dilative behaviour at a small stain. The softening behaviour observed for the eroded specimens is attributed to the eroded soil mass and the increase in void ratio, as formerly reported by Muir Wood et al. (2010), Hicher (2013), and Ke and Takahashi (2014b, 2015). However, the effect of the spatial distribution of the surviving fine particles induced by suffusion may produce a heterogeneous specimen, as demonstrated by Nguyen et al. (2019), and can influence the post-suffusion mechanical response, as discussed by Li et al. (2020). Further investigation of this aspect is necessary.

The deviator stress and pore water pressure against the axial strain at small strain levels up to 1.2% are illustrated in Fig. 10. Interestingly, the eroded specimens seem to show signs of a structural breakdown or collapse. There are sudden drops in deviator stress, and then a sudden increase in pore water pressure is detected at an axial strain of around 0.4% – 1.0% near the peak in all the eroded specimens, whereas those trends do not appear in non-eroded specimen WOE. The sudden changes in these variables are more apparent in specimen WE_N5, which has the largest eroded soil mass. The amount of drop-off in strength appears to be related to the eroded mass loss, which can be converted to a global void ratio after erosion. This suggests that once suffusion occurs, an unstable granular structure or collapsible structure will be formulated by the loss

of fine particles. Under compression conditions, a sudden collapse of the structure will occur instantly. The unstable coarse particle packing may be rearranged into better contacts and may fall into the void spaces.

A detailed investigation of the undrained mechanical behaviour could be helpful for gaining an understanding of the influence of suffusion on the soil mechanical responses. In the following, the undrained characteristics of the soil mechanical behaviour, including the secant stiffness, peak strength, quasi-steady state, instability potential, and flow potential, are discussed in order.

5.1.2. Undrained secant stiffness

The undrained secant stiffness (E_s), within an axial strain of 1.0%, is examined for the non-eroded and eroded specimens, as shown in Fig. 11. In general, the stiffness decreases with straining. The eroded specimens show smaller secant stiffness than the non-eroded specimens. In some eroded specimens, sudden drops in secant stiffness are observed at axial strain levels of around 0.4–0.6%. The
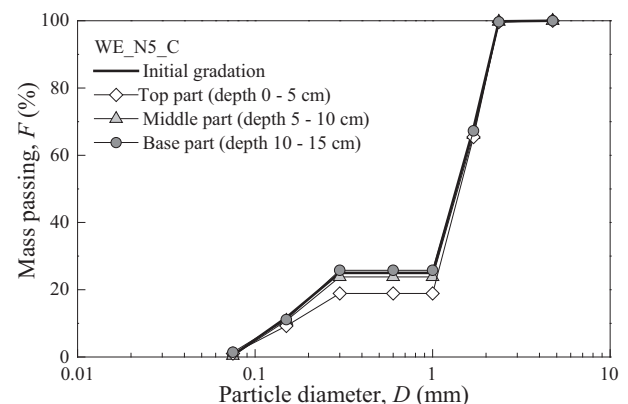

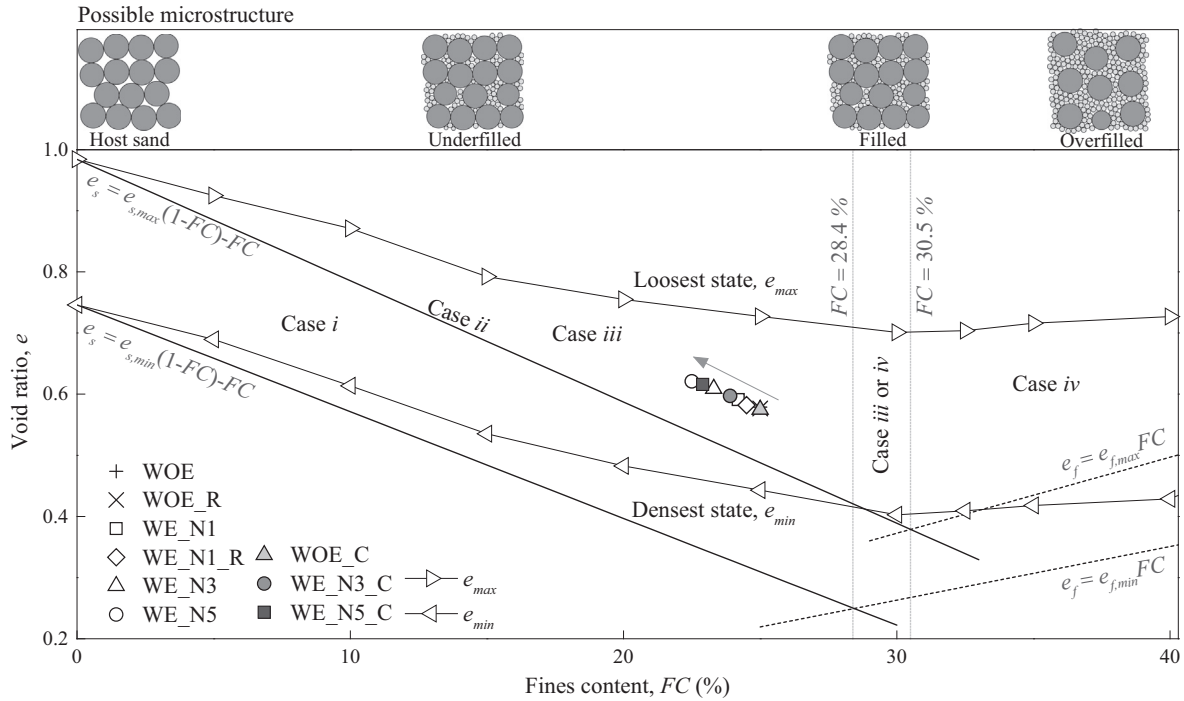Fig. 7. Initial gradation and post-suffusion gradations for WE_N5_C.

Fig. 8. Intergranular matrix phase diagram of tested soils.

shear stiffness is smaller for larger e_e, constant e_{se}, and smaller FC_e.

5.1.3. Undrained peak strength

The undrained peak shear strength (s_p) is the state at which the deviator stress reaches the initial peak in the stress–strain curve, as expressed by Eq. (9) (Ishihara, 1993). Fig. 12 shows the variations in s_p against e_e for all specimens. The peak strength is seen to decrease as suffusion develops, coincident with increasing e_e and constant e_{se}. Multiple suffusions would increase the size of real voids among coarse particles, leading to the contact force between those particles getting smaller, and consequently, the eroded specimens showing larger compressibility. This suggests that suffusion causes the soil structure to become looser and, as a result, it is more likely to collapse. The decrease in shear strength observed for the eroded specimens might be an index of the loss of mass and the increased void ratio.

$$s_p = \frac{q_p}{2} \tag{9}$$

where q_p is the shear stress at the undrained peak state.

5.1.4. Quasi-steady state and residual strength

The quasi-steady state is the state at which the deviator stress shows a minimum value after the initial peak in the stress–strain curve, as expressed by Eq. (10). The quasi-steady-state appears when a soil exhibits strain-softening behaviour during undrained compression at a relatively large strain. Residual strength (s_r) is defined as the shear stress at the quasi-steady stage (q_{ss}) (Ishihara, 1993). As

can be observed from Fig. 9, the soil exhibits the quasi-steady state. Fig. 13 shows the variations in s_r against e_e for all specimens. The s_r of the eroded specimens is significantly smaller than that of the non-eroded specimens, and is almost the same irrespective of N_s, e_e, and e_{se}.

$$s_r = \frac{q_{ss}}{2}\cos\phi_s = \frac{M_{ss}}{2}\cos\phi_s \left(p'_{ss} \right) \tag{10}$$

$$M_{ss} = \frac{6\sin\phi_s}{3 - \sin\phi_s} \tag{11}$$

where M_{ss} is the shear stress ratio at the quasi-steady state (q_{ss}/p'_{ss}), p'_{ss} is the mean effective stress at the quasi-steady state, and ϕ_s is the angle of shearing resistance at the quasi-steady state.

5.1.5. Instability potential

The instability potential of soil, as defined by Lade (1993), is found in the region between the critical state line (CSL) and the instability line (IL). The correlation between the peak shear stress ratio (q_p/p'_p) and the void ratio is called the instability curve by Chu and Leong (2004). Fig. 14a shows the q-p' relation of the eroded and non-eroded specimens superimposed with CSL and ILs. It is observed that the q-p' of all the specimens finally ends up on the same CSL, which agrees with Yang et al. (2006a) for sand-silt mixtures with various non-plastic fines contents. Fig. 14b shows the instability curve for the tests. The peak shear stress ratio that corresponds to the onset of instability is seen to decrease with an increase in e_e with a constant e_{se}, resulting in a larger zone of potential instability. A similar observation was reported by Chu and
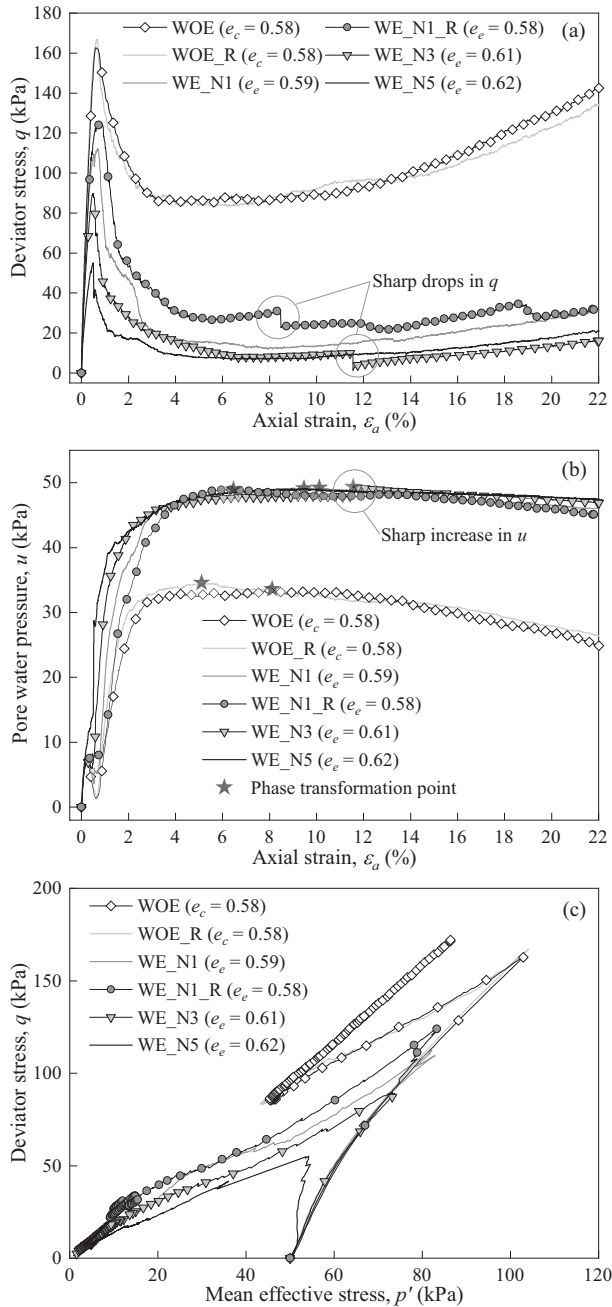
Fig. 9. Undrained compression test results: a) deviator stress versus axial strain, b) pore water pressure versus axial strain, and c) deviator stress versus mean effective stress.

Leong (2004). This suggests that an increase in the void ratio due to multiple seepage-induced suffusion can lead to instability.

5.1.6. Flow potential

The flow potential (u_f) denotes the maximum pore water pressure reached in undrained conditions, which can be used as an indicator for characterising the flow failure phenomenon of sands, as expressed by Eq. (12) (Yoshimine and Ishihara, 1998). Unstable deformation and flow failure can occur when the residual strength stays at the critical

steady-state. The flow potential corresponds to the stress state at the phase transformation proposed by Ishihara et al. (1975). In general, the value of u_f is equal to 100% for a larger void ratio and approaches 0% for a smaller void ratio. If $u_f = 100\%$, the soil will liquefy with no residual strength, and flow deformation will continuously occur.

$$u_f = \left(1 - \frac{p'_{pts}}{p'_i}\right) \times 100\% \qquad (12)$$

where p'_{pts} is the mean effective stress at the phase transformation state.

Fig. 15 shows the values for u_f plotted against e_e for all specimens. u_f significantly increases with an increasing e_e. The larger flow potential with the increasing void ratio agrees with Yoshimine and Ishihara (1998). Their experimental results for Toyoura sand indicate that the values for u_f are sensitive to density and mean effective stress. For a given mean effective stress, the value for u_f increases with an increasing void ratio. When the initial mean effective stress is small (i.e., $p'_i = 50$ kPa), a slight increase in void ratio causes a large increase in the flow potential accompanied by a decrease in residual strength. Therefore, the increasing void ratio induced by suffusion causes the soil to be more unstable, leading to a collapse of the soil structure and flow failure.

5.2. Multistage undrained cyclic responses

The multistage undrained cyclic shearing test is performed on the specimen without erosion, and on two specimens with erosion with three and five seepage cycles, named WOE_C, WE_N3_C, and WE_N5_C, respectively. A summary of the multistage undrained cyclic shearing test results is tabulated in Table 6. The void ratios before shearing (e_e) and after reconsolidation, following the undrained cycle shearing (e_r), are also shown in the table. Changes in the void ratio during the first consolidation, seepage, and undrained shearing, followed by reconsolidation, are shown in Fig. 16. Due to suffusion, the eroded specimens have larger e_e before the multistage cyclic shearing test, and e_e becomes greater with N_s. For each reconsolidation stage, the changes in e_r of the eroded specimens are significantly larger than those of the non-eroded specimen and are larger with N_s. These results suggest that eroded soils with larger void ratios before shearing have larger compressibility.

The cyclic behaviour of the specimens under the *CSR* of 0.10 is presented in Fig. 17. All cyclic shearing responses exhibit incremental build-up of shear strain and excess pore water pressure. All specimens show increases in both r_u and cyclic axial strain amplitude with an increasing number of loading cycles. e_c and e_s are 0.57 and 1.10 for specimen WOE_C after consolidation, and e_e is 0.60 and 0.62 with the same e_{se} of 1.10 for specimens WE_N3_C and WE_N5_C after erosion, respectively. The eroded specimens with larger e_e and the same e_{se} are less cyclic-

Table 5
Summary of main parameters of undrained monotonic tests.

Test code	FC or FC_e (%)	e_c or e_e	e_s or e_{se}	D_{rc} or D_{re} (%)	p'_i (kPa)	q_p (kPa)	q_{ss} (kPa)	p'_p (kPa)	p'_{ss} (kPa)	M_{ss} (ϕ_s)	s_p (kPa)	s_r (kPa)	p'_{pts} (kPa)	u_f (%)	Stress path
WOE	25.0	0.58	1.10	53	50	163	85	103	46	1.87 (45.5°)	81	30	45	10	C–D
WOE_R	25.0	0.58	1.10	54	50	167	83	104	43	1.92 (46.7°)	84	28	43	14	C–D
WE_N1	24.2	0.59	1.10	49	50	112	12	82	5	2.36 (57.8°)	56	3	5	90	C
WE_N1_R	24.5	0.58	1.10	52	50	125	26	84	10	2.55 (63.5°)	62	6	9	82	C
WE_N3	23.3	0.61	1.10	42	50	90	8	73	5	1.64 (40.1°)	45	3	1	98	C
WE_N5	22.5	0.62	1.09	38	50	55	7	54	4	1.90 (46.3°)	28	2	3	94	C

Note: C is contraction, C–D is contraction–dilation.

resistant than the non-eroded specimen with smaller e_e and the same e_{se}. The constant inter-coarse void ratio with an increasing global void ratio means that the loss of fine particles increases the void volume of the coarse particles during the erosion process, leading to larger inter-coarse voids. Interestingly, sudden changes in r_u and p' can be observed in Fig. 17 during cyclic shearing for the eroded specimens. This response confirms that suffusion creates an unstable structure in eroded soils. Upon cyclic shearing, the structure suddenly breaks down, triggering a sudden increase in excess pore water pressure generation.

The cyclic resistance curves, $CSR - N_{ru=0.8}$, for the non-eroded and eroded specimens, are plotted in Fig. 18 along with the estimated relative density before each shearing. The results are fitted as $CSR = aN^{-b}$, where a and b are fitting parameters. The results show that the cyclic resistance of the eroded specimens is significantly smaller than that of the non-eroded specimen and that it gets smaller with increases in e_e and N_s, which coincides with the soil density. This suggests that multiple seepage-induced suffusion does make the soil looser, resulting in a higher liquefaction potential. However, more data are needed to explore and confirm this cyclic behaviour.

5.3. Discussions on impact of suffusion on undrained mechanical responses

Seepage-induced internal instability is a coupled process of an eroded soil mass, change in volume, and change in hydraulic conductivity. Combining these variables is necessary to distinguish the internal instability phenomena: suffosion and suffusion (Fannin and Slangen, 2014). The combination can also be used to postulate the impact of the instabilities on the undrained mechanical behaviour. Indeed, the effect of suffosion on the soil responses has already been reported in the literature (Xiao and Shwiyhat, 2012; Ke and Takahashi, 2014a; Ouyang and Takahashi, 2015; Mehdizadeh et al., 2017a, 2017b; Mehdizadeh et al., 2019). Suffosion seems to provide a positive impact on soils in terms of undrained compression and cyclic resistance.

The influence of internal erosion on the soil behaviour during cyclic loading and the monotonic shearing of internally unstable soil has been well-documented in Mehdizadeh et al. (2017a). The authors investigated the effect of internal erosion on angular gap-graded sand with a 25% fines content, in which a seepage-induced eroded mass loss of 66% of the initial fines content, accompanied by a marked volumetric strain of 2.75%, was observed. The mass loss accompanied by a noticeable volumetric change matches the suffosion mode (Fannin and Slangen, 2014). The mechanical response demonstrated that this destructive phenomenon causes the initial undrained peak shear strength to increase and is accompanied by a decrease in the maximum induced pore water pressure. Larger cyclic resistance was also observed in the eroded soil. The destruction is attributed to the local particle redisposition
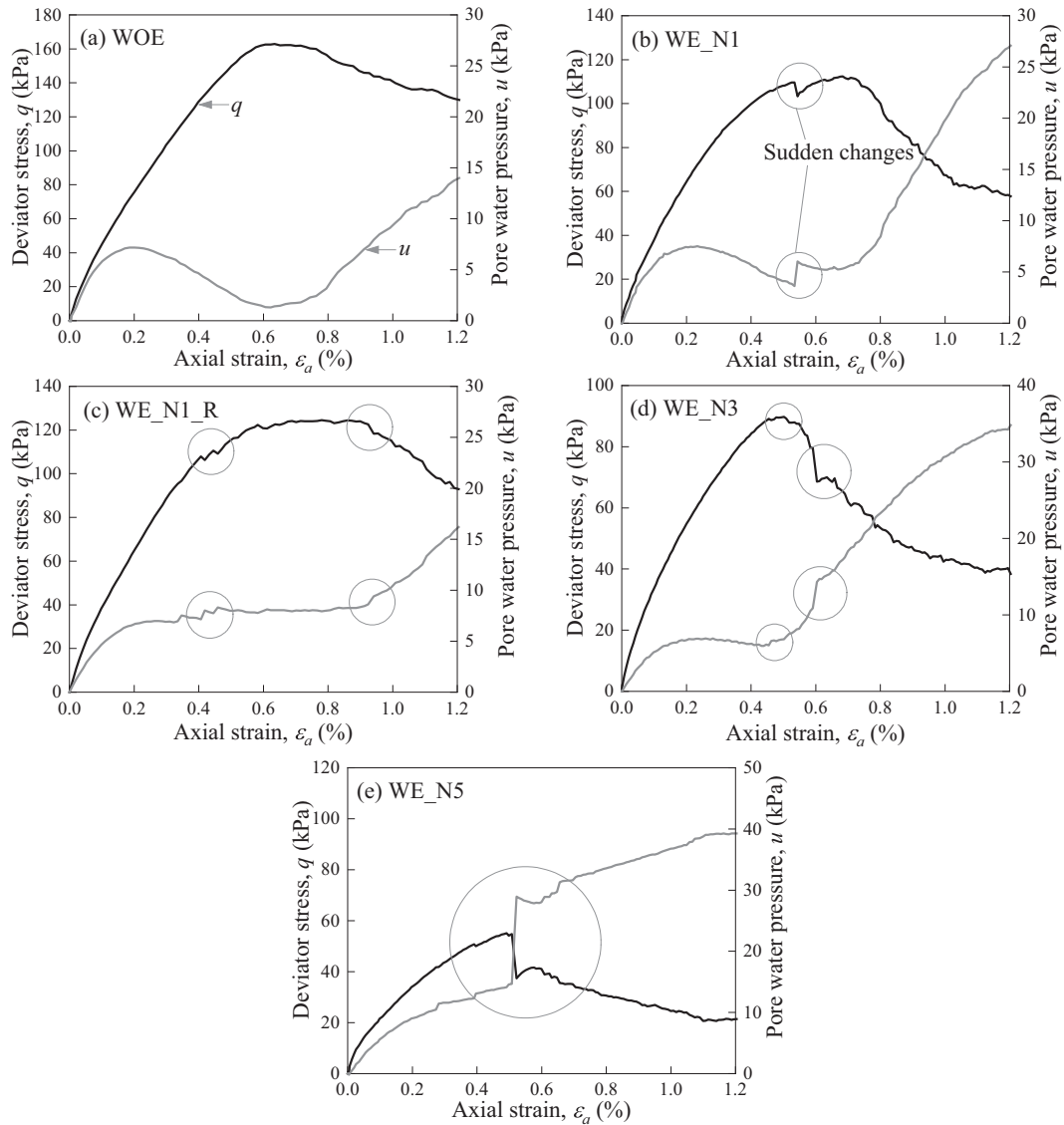
Fig. 10. Changes in deviator stress, pore water pressure, and radial strain against small axial strain up to 1.2%.

caused by a localised jet flow, a kind of piping in the specimen, resulting in a large loss of fine particles and a marked change in volume (Ke and Takahashi, 2014b). This implies that the rearrangement of the soil structure lets the coarse particles come into better contact and appears to improve the soil strength.

In comparison to suffosion, there is a higher possibility that suffusion can induce a reduction of the soil strength as the finer particles can erode with no loss in the matrix integrity of the coarse particle skeleton. In this study, the results of suffusion tests on angular gap-graded sand with a 25% fines content indicate a non-destructive response, as a seepage-induced eroded soil mass without a marked change in volume accompanies a change in hydraulic conductivity which is termed suffusion (Fannin and Slangen, 2014). The triaxial compression test results show that this non-destructive response leads the soil to a looser state.
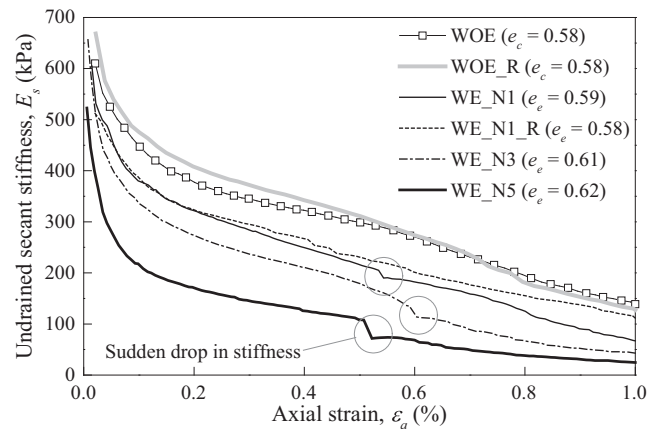
Fig. 11. Secant stiffness of eroded and non-eroded specimens at small axial strain up to 1.0%.
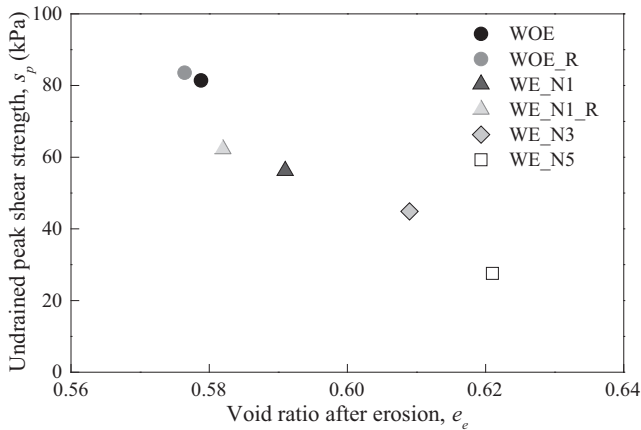
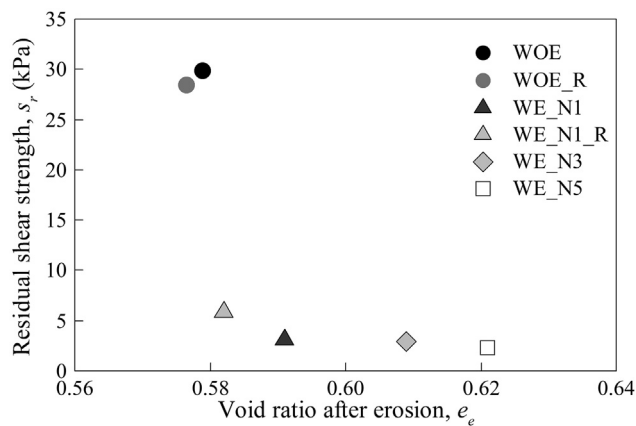Fig. 12. Peak strength against void ratio.

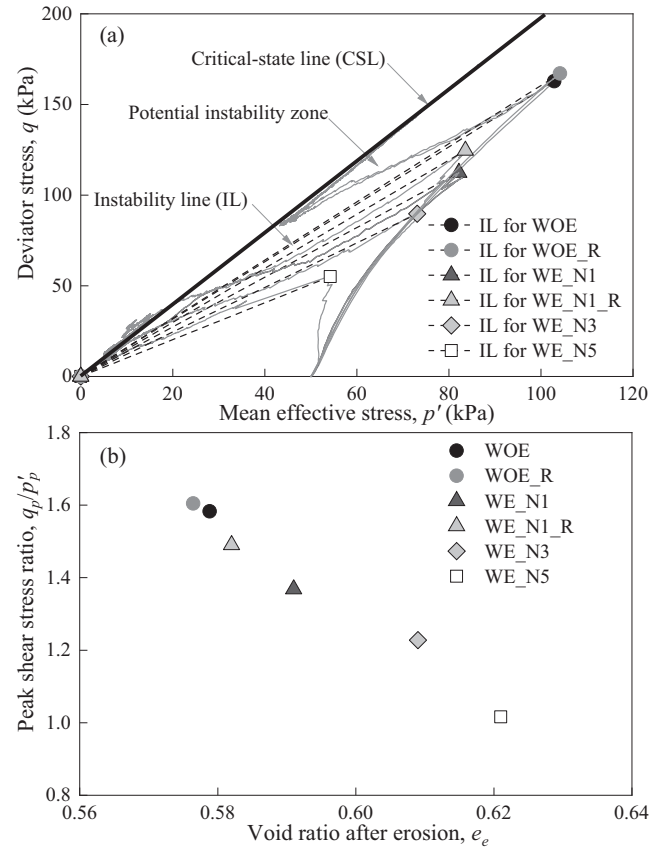Fig. 13. Residual strength against void ratio.

Fig. 14. Instability potential (a) determination of instability zone and (b) stress ratio of instability line against void ratio.
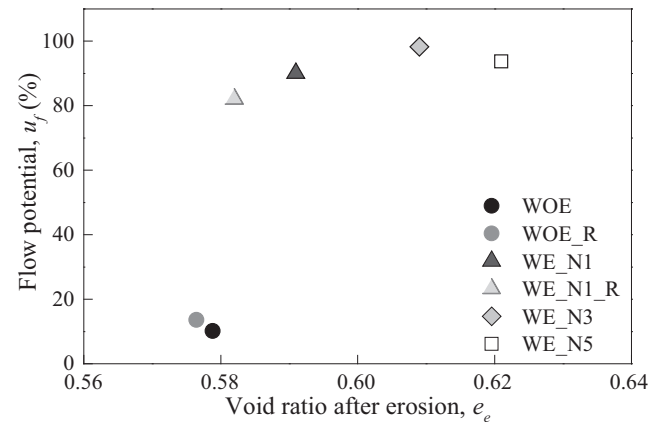

Fig. 15. Flow potential against void ratio.

In virtually all cases, the eroded soil has smaller shear strength and shows more contractive response than the non-eroded soil, although the eroded soil mass is relatively small (*i.e.*, a maximum eroded mass loss of 12.8% of the initial fines content). Suffusion also decreases the small strain, namely, the undrained stiffness of the soil. The same is true in undrained cyclic shearing. Additionally, there is a sign of an unstable or collapsible structure in the soil induced by suffusion. This is most likely because the migration of fine particles induced by the seepage flow causes localised heterogeneity and differences in the microstructure in terms of the void ratio and load distribution throughout the soil, but it does not change the coarser skeleton of the soil. However, microstructural observations would help to confirm these hypotheses. The observation suggests that suffusion would be a severe concern in the long-term stability of earthen structures. The findings in this study will be helpful for managing the associated risk of suffusion in earthen structures, which could then then be managed in a different way than the risk of suffosion.

6. Conclusions

A series of suffusion experiments was carried out to investigate suffusion development under multiple seepage conditions and its impact on the undrained mechanical behaviour of internally eroded soil under monotonic and cyclic loading conditions. A multiple seepage test procedure was proposed for investigating complex suffusion development, which produced repeatable results. Suffusion

Table 6
Summary of main parameters of multistage undrained cyclic tests.

Test code	Before shearing		$CSR = 0.10$		After re-consolidation		$CSR = 0.15$		After re-consolidation		$CSR = 0.20$	
	e_e (−)	D_r (%)	$N_{ru=0.8}$ (−)	ε_{af} (%)	e_r (−)	D_r (%)	$N_{ru=0.8}$ (−)	ε_{af} (%)	e_r (−)	D_r (%)	$N_{ru=0.8}$ (−)	ε_{af} (%)
WOE_C	0.57	54	229	0.10	0.57	56	41	0.28	0.56	58	7	−0.31
WE_N3_C	0.60	46	113	0.11	0.59	49	12	−0.48	0.57	56	1.5	−0.34
WE_N5_C	0.62	39	95	−0.75	0.60	45	1.5	−2.50	0.58	52	−	−2.51

Note: + is compression, − is extension.

exhibited a non-destructive response as a seepage-induced eroded soil mass without a marked change in volume and with a change in hydraulic conductivity. The suffusion process was seen to induce local clogging of the detached particles accompanied by variations in the discharge velocity and hydraulic gradient, indicating the necessity for both variations when evaluating hydraulic loading.

The intergranular matrix phase diagram helped postulate the microstructure of the internally unstable soil. The underfilled soil, having a coarse-dominated microstructure, was found to be highly susceptible to suffusion, which can be initiated at small hydraulic gradients, as the unstressed finer particles can migrate through the voids of the coarser particles by seepage flow without any change in the soil structure.

Multiple seepage-induced suffusion was seen to significantly affect the undrained mechanical behaviour of the soil. The eroded soil became looser as a consequence of the loss of the finer fraction without disturbing the coarse skeleton. The shear strength, residual strength, and stiffness showed significant decreases after suffusion. The eroded soil was prone to higher liquefaction and flow failure potentials. The shear strength consistently decreased with increases in the amount of eroded soil mass and the global void ratio, but was constant in the inter-coarse void ratio. These variables can be used as indicators when predicting the post-suffusion mechanical behaviour of internally unstable soil.

Suffusion creates a loose material structure, as demonstrated by the sudden drops in shear stress and stiffness with a sharp increase in pore water pressure. This might be considered an indication of the deterioration of the unstable soil packing. As eroded soil is already unstable, the disturbance caused by cyclic loading produces the collapse of the soil, leading to lower resistance to liquefaction.

The observed decreases in strength, stiffness, and liquefaction resistance of the eroded soil indicated how dangerous suffusion is to the mechanical behaviour of the soil. The authors' highlights of the effect of internal erosion should be included when evaluating the shear strength and cyclic resistance in order to assess the internal stability state of an earthen structure. However, the findings of this study have the following limitations: (1) the specimens were tested with only one non-plastic gap-graded gradation curve and one relative density; (2) the isotropic stress state

was considered, as opposed to those in the field, which are likely to be under anisotropic stress; (3) downward seepage flow was imposed in the tests, which may differ from the flow conditions in the field; and (4) the magnitude of the
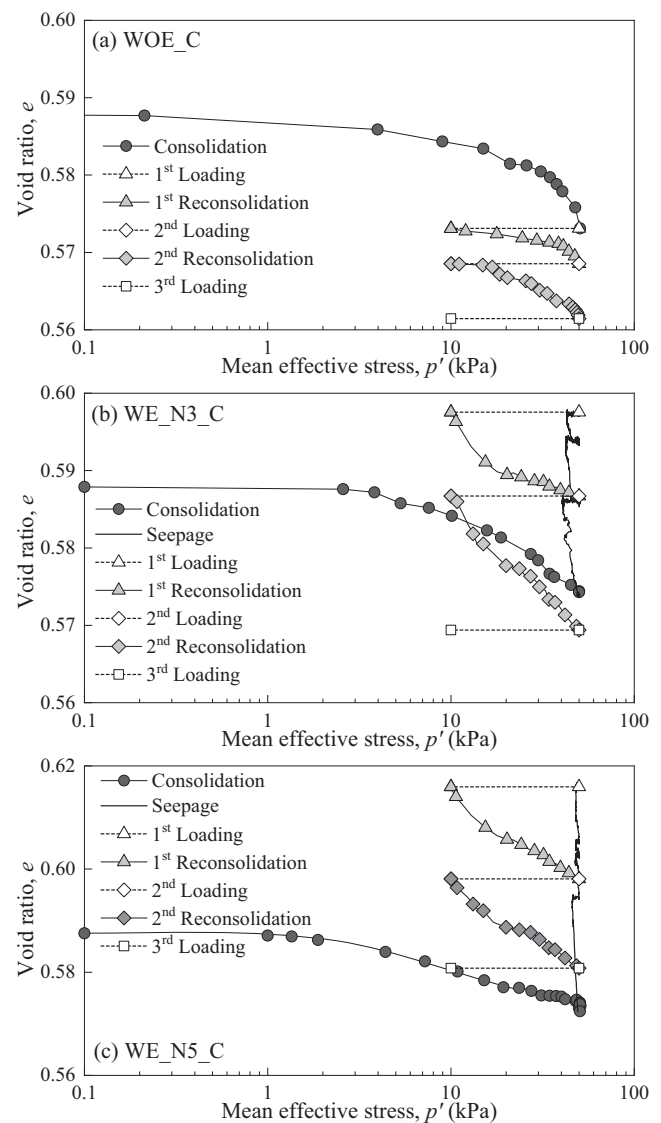

Fig. 16. Void ratio against mean effective stress for multiple cyclic triaxial shearings and reconsolidations for (a) WOE_C, (b) WE_N3_C, and (c) WE_N5_C.
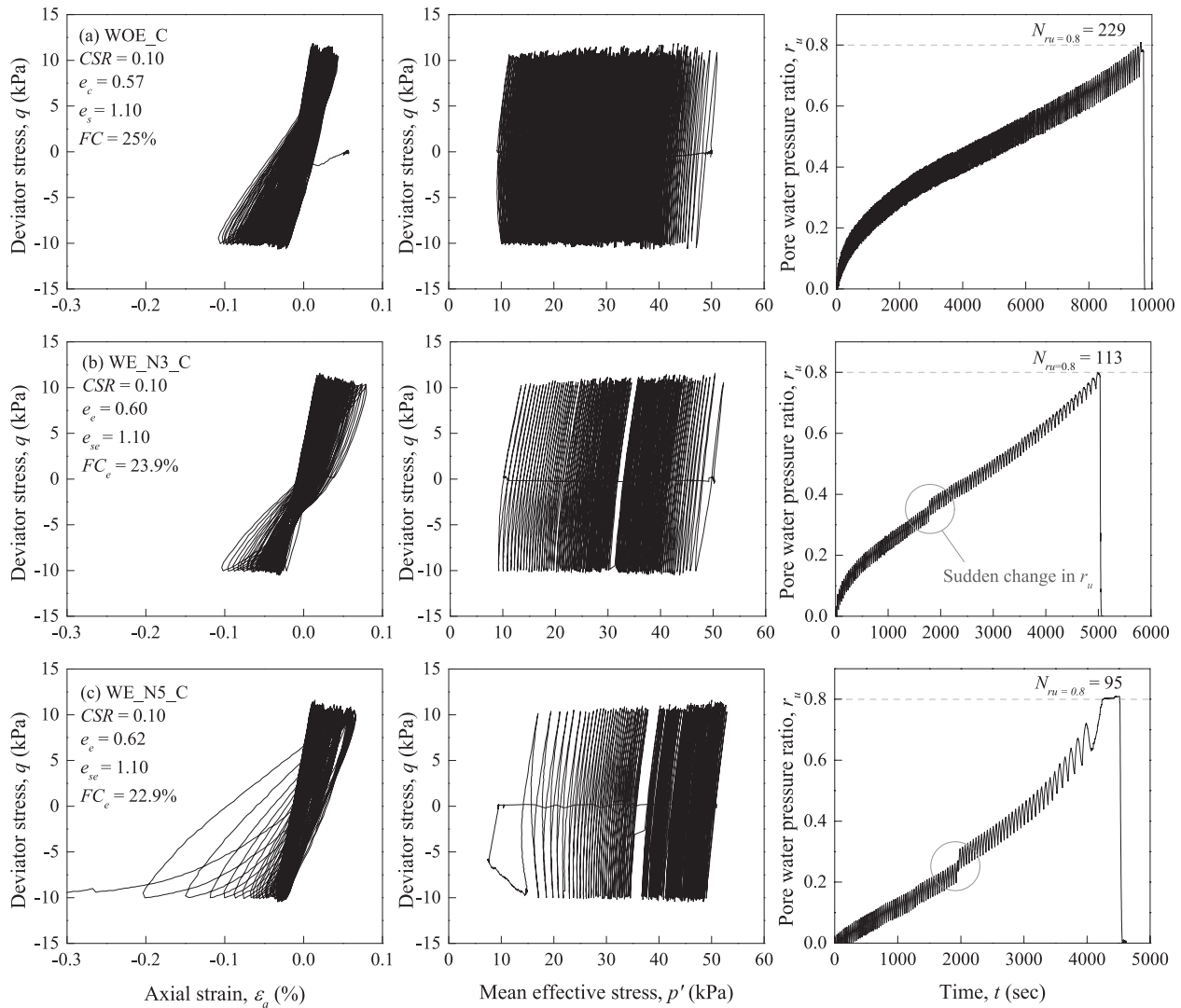
Fig. 17. Cyclic deviator stress against axial strain, deviator stress versus mean effective stress, and cyclic pore water pressure ratio versus number of cycle for (a) WOE_C, (b) WE_N3_C, and (c) WE_N5_C subjected to CSR = 0.10.

hydraulic gradient in this experiment may be higher than those in the field. Many factors affect the in-situ internal erosion behaviour of natural deposits, which were not explicitly studied in this study. More advanced laboratory testing with various gradation curves (i.e., gap-graded soil with different gap ratios and fines contents, and widely graded soils) at various environmental conditions (i.e., density, confining stress, seepage direction, and hydraulic loading pattern) in a triaxial erosion apparatus with well-documented data during internal erosion and on the post-erosion mechanical responses, would be worthwhile to better predict the internal erosion and its consequences. Nonetheless, it is believed that the findings of this study will contribute to a better understanding of suffusion and how it affects the soil mechanical behaviour, which will help with the risk and safety assessments of earthen structures against internal erosion.
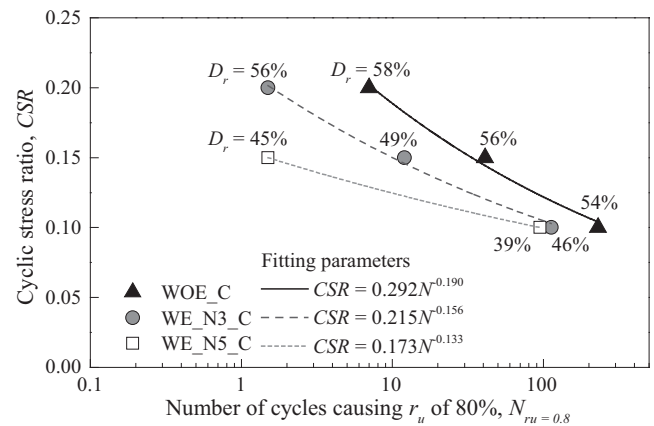

Fig. 18. Cyclic shearing resistance curves of eroded and non-eroded specimens.

Acknowledgements

References

ASTM D2487-11, 2012. Standard practice for classification of soils for engineering purposes (Unified Soil Classification System). Annual Book of ASTM Standards. ASTM International, West Conshohocken, PA.

Bendahmane, F., Marot, D., Alexis, A., 2008. Experimental parametric study of suffusion and backward erosion. J. Geotech. Geoenviron. Engng. 134 (1), 57–67.

Bouferra, R., Benseddiq, N., Shahrour, I., 2007. Saturation and preloading effects on the cyclic behavior of sand. Int. J. Geomech. 7 (5), 396–401.

Chang, D.S., Zhang, L.M., 2011. A stress-controlled erosion apparatus for studying internal erosion in soils. Geotech. Testing J. 34 (6), 579–589.

Chu, J., Leong, W.K., 2004. Effect of fines on instability behaviour of loose sand. Géotechnique 52 (10), 751–755.

Fannin, R.J., Slangen, P., 2014. On the distinct phenomena of suffusion and suffosion. Géotechnique Lett. 4 (4), 289–294.

Hicher, P.-Y., 2013. Modelling the impact of particle removal on granular material behaviour. Géotechnique 63 (2), 118–128.

Ishihara, K., 1993. Liquefaction and flow failure during earthquakes. Géotechnique 43 (3), 351–451.

Ishihara, K., Okada, S., 1982. Effects of large preshearing on cyclic behavior of sand. Soils Found. 22 (3), 109–125.

Ishihara, K., Tatsuoka, F., Yasuda, S., 1975. Undrained deformation and liquefaction of sand under cyclic stresses. Soils Found. 15 (1), 29–44.

Jiang, M.J., Konrad, J.M., Leroueil, S., 2003. An efficient technique for generating homogeneous specimens for DEM studies. Comput. Geotech. 30 (7), 579–597.

Jiang, N.-J., Soga, K., 2017. The applicability of microbially induced calcite precipitation (MICP) for internal erosion control in gravel–sand mixtures. Géotechnique 67 (1), 42–55.

Ke, L., Takahashi, A., 2012. Strength reduction of cohesionless soil due to internal erosion induced by one-dimensional upward seepage flow. Soils Found. 52 (4), 698–711.

Ke, L., Takahashi, A., 2014a. Triaxial erosion test for evaluation of mechanical consequences of internal erosion. Geotech. Testing J. 37 (2), 20130049. https://doi.org/10.1520/GTJ20130049.

Ke, L., Takahashi, A., 2014b. Experimental investigations on suffusion characteristics and its mechanical consequences on saturated cohesionless soil. Soils Found. 54 (4), 713–730.

Ke, L., Takahashi, A., 2015. Drained monotonic responses of suffusional cohesionless soils. J. Geotech. Geoenviron. Engng 141 (8), 04015033. https://doi.org/10.1061/(ASCE)GT.1943-5606.0001327.

Kenney, T.C., Lau, D., 1985. Internal stability of granular filters. Can. Geotech. J. 22 (2), 215–225.

Kenney, T.C., Lau, D., 1986. Internal stability of granular filters: Reply. Can. Geotech. J. 23 (3), 420–423.

Kézdi, A., 1979. Soil Physics: Selected Topics. Elsevier Scientific Publishing Co., Amsterdam.

Ladd, R.S., 1978. Preparing test specimens using undercompaction. Geotech. Test. J. 1 (1), 16. https://doi.org/10.1520/GTJ10364J.

Lade, P.V., 1993. Initiation of static instability in the submarine Nerlerk berm. Can. Geotech. J. 30 (6), 895–904.

Lade, P.V., Liggio, C.D., Yamamuro, J.A., 1998. Effects of non-plastic fines on minimum and maximum void ratios of sand. Geotech. Testing J. 21 (4), 336. https://doi.org/10.1520/GTJ11373J.

Lafleur, J., Mlynarek, J., Rollin, A.L., 1989. Filtration of broadly graded cohesionless soils. J. Geotech. Geoenviron. Engng 115 (12), 1747–1768.

Li, S., Russell, A.R., Muir Wood, D., 2020. Influence of particle-size distribution homogeneity on shearing of soils subjected to internal erosion. Can. Geotech. J. 57 (11), 1684–1694.

Luo, Y.-L., Qiao, L., Liu, X.-X., Zhan, M.-L., Sheng, J.-C., 2013. Hydromechanical experiments on suffusion under long-term large hydraulic heads. Nat. Hazards 65 (3), 1361–1377.

Hu, Z., Zhang, Y., Yang, Z., 2020. Suffusion-induced evolution of mechanical and microstructural properties of gap-graded soils using CFD-DEM. J. Geotech. Geoenviron. Engng 146 (5), 04020024. https://doi.org/10.1061/(ASCE)GT.1943-5606.0002245.

Marot, D., Bendahmane, F., Rosquoet, F., Alexis, A., 2009. Internal flow effects on isotropic confined sand-clay mixtures. Soil Sediment Contam. 18 (3), 294–306.

Marot, D., Rochim, A., Nguyen, H.-H., Bendahmane, F., Sibille, L., 2016. Assessing the susceptibility of gap-graded soils to internal erosion: proposition of a new experimental methodology. Nat. Hazards 83 (1), 365–388.

Mehdizadeh, A., Disfani, M.M., Evans, R., Arulrajah, A., Ong, D.E.L., 2017a. Mechanical consequences of suffusion on undrained behaviour of a gap-graded cohesionless soil-an experimental approach. Geotech. Testing J. 40 (6), 20160145. https://doi.org/10.1520/GTJ1711-EB10.1520/GTJ20160145.

Mehdizadeh, A., Disfani, M.M., Evans, R., Arulrajah, A., 2017b. Progressive internal erosion in a gap-graded internally unstable soil: mechanical and geometrical effects. Int. J. Geomech. 18 (3), 04017160. https://doi.org/10.1061/(ASCE)GM.1943-5622.0001085.

Mehdizadeh, A., Disfani, M.M., Evans, R., Arulrajah, A., 2019. Impact of suffusion on the cyclic and post-cyclic behaviour of an internally unstable soil. Géotechnique Lett. 9 (3), 218–224.

Mitchell, J.K., Soga, K., 2005. In: Fundamentals of Soil Behavior, Vol. 3. John Wiley and Sons, Hoboken, NJ.

Moffat, R.A., Fannin, R.J., 2006. A large permeameter for study of internal stability in cohesionless soils. Geotech. Testing J. 29 (4), 273–279.

Moffat, R., Fannin, R.J., Garner, S.J., 2011. Spatial and temporal progression of internal erosion in cohesionless soil. Can. Geotech. J. 48 (3), 399–412.

Muir Wood, D., Maeda, K., Nukudani, E., 2010. Modelling mechanical consequences of erosion. Géotechnique 60 (6), 447–457.

Nguyen, C.D., Benahmed, N., Andò, E., Sibille, L., Philippe, P., 2019. Experimental investigation of microstructural changes in soils eroded by suffusion using X-ray tomography. Acta Geotechnica 14 (3), 749–765.

Ouyang, M., Takahashi, A., 2015. Influence of initial fines content on microstructure of soils subjected to internal erosion. Can. Geotech. J. 53, 299–313.

Prasomsri, J., Takahashi, A., 2020. The role of fines on internal instability and its impact on undrained mechanical response of gap-graded soils. Soils Found. 60 (6), 1468–1488.

Reddi, L.N., Lee, I.M., Bonala, M.V., 2000. Comparison of internal and surface erosion using flow pump tests on a sand-kaolinite mixture. Geotech. Testing J. 23 (1), 116–122.

Richards, K.S., Reddy, K.R., 2008. Experimental investigation of piping potential in earthen structures. Geocongress 2008: geosustainability and geohazard mitigation, pp. 367–376.

Rochim, A., Marot, D., Sibille, L., Thao Le, V., 2017. Effects of hydraulic loading history on suffusion susceptibility of cohesionless soils. J. Geotech. Geoenviron. Engng 143 (7), 04017025. https://doi.org/10.1061/(ASCE)GT.1943-5606.0001673.

Sail, Y., Marot, D., Sibille, L., Alexis, A., 2011. Suffusion tests on cohesionless granular matter: experimental study. Eur. J. Environ. Civil Eng. 15 (5), 799–817.

Scholtès, L., Hicher, P.-Y., Sibille, L., 2010. Multiscale approaches to describe mechanical responses induced by particle removal in granular materials. Comptes Rendus Mécanique 338 (10-11), 627–638.

Sherard, J.L., Dunnigan, L.P., Talbot, J.R., 1984. Basic properties of sand and gravel filters. J. Geotech. Engng ASCE 110 (6), 684–700.

Shire, T., O'Sullivan, C., 2016. Constriction size distributions of granular filters: a numerical study. Géotechnique. 66 (10), 826–839.

Shire, T., O'Sullivan, C., Hanley, K.J., Fannin, R.J., 2014. Microstructure and effective stress distribution in internally unstable soils. J. Geotech. Geoenviron. Engng 140 (12), 04014072.

Skempton, A.W., Brogan, J.M., 1994. Experiments on piping in sandy gravels. Géotechnique 44 (3), 449–460.

Slangen, P., Fannin, R.J., 2017. A flexible wall permeameter for investigating suffusion and suffosion. Geotech. Testing J. 40 (1), 1–14.

Tanaka, T., Toyokuni, E., 1991. Seepage-failure experiments on multi-layered sand columns: effects of flow conditions and residual effective stress on seepage-failure phenomena. Soils Found. 31 (4), 13–36.

Thevanayagam, S., Mohan, S., 2000. Intergranular state variables and stress–strain behaviour of silty sands. Géotechnique 50 (1), 1–23.

Towhata, I., Ishihara, K., 1985. Undrained strength of sand undergoing cyclic rotation of principal stress axes. Soils Found. 25 (2), 135–147.

Wan, C.F., Fell, R., 2008. Assessing the potential of internal instability and suffusion in embankment dams and their foundations. J. Geotech. Geoenviron. Engng 134 (3), 401–407.

Xiao, M., Shwiyhat, N., 2012. Experimental investigation of the effects of suffusion on physical and geomechanic characteristics of sandy soils. Geotech. Testing J. 35 (6), 890–900.

Xiong, H., Wu, H., Bao, X., Fei, J., 2021a. Investigating effect of particle shape on suffusion by CFD-DEM modeling. Constr. Build. Mater. 289, 123043. https://doi.org/10.1016/j.conbuildmat.2021.123043.

Xiong, H., Yin, Z.-Y., Zhao, J., Yang, Y., 2021b. Investigating the effect of flow direction on suffusion and its impacts on gap-graded granular soils. Acta Geotech. 16 (2), 399–419.

Yang, J., Yin, Z.-Y., Laouafa, F., Hicher, P.-Y., 2019a. Analysis of suffusion in cohesionless soils with randomly distributed porosity and fines content. Comput. Geotech. 111, 157–171.

Yang, J., Yin, Z.-Y., Laouafa, F., Hicher, P.-Y., 2019b. Modeling coupled erosion and filtration of fine particles in granular media. Acta Geotech. 14 (6), 1615–1627.

Yang, J., Yin, Z.-Y., Laouafa, F., Hicher, P.-Y., 2020. Hydromechanical modeling of granular soils considering internal erosion. Can. Geotech. J. 57 (2), 157–172.

Yang, S.L., Sandven, R., Grande, L., 2006a. Steady-state lines of sand–silt mixtures. Can. Geotech. J. 43 (11), 1213–1219.

Yang, S., Lacasse, S., Sandven, R., 2006b. Determination of the transitional fines content of mixtures of sand and non-plastic fines. Geotech. Testing J. 29 (2), 14010. https://doi.org/10.1520/GTJ14010.

Yin, Z.-Y., Huang, H.-W., Hicher, P.-Y., 2016. Elastoplastic modeling of sand–silt mixtures. Soils Found. 56 (3), 520–532.

Yoshimine, M., Ishihara, K., 1998. Flow potential of sand during liquefaction. Soils Found. 38 (3), 189–198.

Zhong, C., Le, V.T., Bendahmane, F., Marot, D., Yin, Z.-Y., 2018. Investigation of spatial scale effects on suffusion susceptibility. J. Geotech. Geoenviron. Engng. 144 (9), 04018067. https://doi.org/10.1061/(ASCE)GT.1943-5606.0001935.